Elastoplastic and limit analysis of reinforced concrete with an equilibrium-based finite element formulation

Mohammed-Khalil Ferradi, Agnès Fliscounakis, Mathieu Arquier, Jeremy Bleyer

Elastoplastic and limit analysis of reinforced concrete with an equilibrium-based finite element formulation

Mohammed-Khalil Ferradi *[1], Agnès Fliscounakis[2], Mathieu Arquier[3], and Jeremy Bleyer[4]

[1]Mohammed VI Polytechnic University, Modeling Simulation and Data Analysis, Benguerir, Morocco
[2]Univ Rennes, INSA Rennes, LGCGM - EA 3913, F-35000 Rennes, France
[3]Strains Engineering, Paris, France
[4]Laboratoire Navier, Ecole des Ponts, Univ Gustave Eiffel, CNRS, 77455 Marne-la-vallée, France

July 10, 2023

Abstract

In this paper, a 3D equilibrium-based finite element formulation is presented for reinforced concrete, where the stress unknowns strongly satisfy the equilibrium equations. The concrete stress tensor is interpolated using tetrahedral piece-wise linear element with statically admissible discontinuities, while the rebars are considered as 1D elements embedded into the concrete, intersecting the triangular mesh. Thus, the global equilibrium is ensured by writing for each face of the mesh the traction continuity equation, while including the rebar stress contribution for the intersected triangular faces. The elastic equilibrium formulation is then written into an equivalent optimization problem, extended to the elastoplastic case by simply adding semi-definite matrix constraints on the concrete stress tensor, corresponding to a Rankine or a truncated Mohr-Coulomb criterion. As for the rebars, they are considered to obey a 1D perfectly elastoplastic behavior. The present formulation is also developed for limit analysis, to directly obtain an estimate of the lower bound of the collapse load. The resulting semi-definite programming optimization problems are solved using a in-house interior point algorithm.

Keywords: Equilibrium finite element method, reinforced concrete, semi-definite programming, limit analysis

1 Introduction:

Reinforced concrete has a complex behavior, mixing ductile reinforcements with the brittle concrete, which makes it a particularly hard subject to address. Unlike the steel material for which the normality flow rule has proved to accord well with reality, it is not obvious to consider reinforced concrete as a perfectly plastic material, which *a priori* prevents the use of powerful mathematical frameworks to deal with non-linearity. However, the study of many test cases showed that the application of the upper bound and lower bound theorem, formulated simultaneously by Gvozdev [AA38] and Drucker [DPG52], makes it possible in many cases to predict load-carrying capacity for concrete structures as illustrated in [NH16]. Actually, this good adequacy strongly depends on several design principals which are not always fulfilled (see [MS72] for a good discussion on the strength and limitation of limit analysis). For instance, a too high ratio of tensile reinforcement can lead to a concrete failure by crushing, which doesn't comply with the plastic flaw behaviour. Conversely, a minimum area of reinforcement is also needed to confer to concrete its plastic behaviour, as required in EN 1992-1-1([En92]). As soon as those requirements are fulfilled, numerous approaches based on perfect plasticity exist in order to evaluate RC structures failure, both manually and numerically, whom a rapid review is done below.

*khalil.ferradi@um6p.ma

First of all, a hand-based calculation can often give a good understanding of the overall problem. Manual methods can roughly be separated into two main families: the lower bound theorem methods and the upper bound theorem methods.

Applying the lower bound theorem and dealing with an RC structure, one can use the strut-and-ties method based on the truss analogy introduced in ([Rit99], [Mö08]) and becoming popular thanks to [SSJ87], making sure that the loading can be in static equilibrium according to a chosen failure criterion. Even if guidelines exist to prevent such mistakes, this method often overlooks, in its everyday life application, the cracking effect on the strut resistance and, more generally, does not ensure that important strains in concrete won't provoke a hasty failure. Another, quite similar, application of the lower bound theorem to design RC structures is the stress fields method. A good description of this method is made in [RM07].

Regarding the upper bound theorem, the yield line theory established by Johansen [Joh72] illustrates how RC structures can be designed with a kinematic point of view, which amounts to overestimating the failure loading by guessing a virtual mechanism where plastic strains only occur along lines. Even so this non-conservative approach could seem unsafe, it gives good results when the proposed mechanism reflects the reality and, furthermore, it procures an appropriate complementary understanding to the strut-and-ties static approach. The numerical extension of those classical manual calculations is at the basis of some nowadays software like LimiteState [2219] (for yield lines) or CAST [TT02] (for strut-and-ties).

In the above developments, a complementarity between the equilibrium stress field and the virtual mechanisms of a collapse load appears. This complementarity is indicative of the strong understanding brought by a dual approach, which proves the necessity of the equilibrium stress field.

Manual approaches reach their limit relatively quickly, as soon as the complexity of the structures or of the loading is outside of the framework of the methods. At this point intervene numerical methods which progressively replace manual design in the engineering world. As for the elastic theory, the numerical methods implemented in current softwares dealing with non-linear reinforced concrete, are mainly based on kinematic formulations. Softwares like Athena [CCJS14] or Diana [D20] are good examples of such kinematic approaches, where the concrete is modeled thanks to 3D finite elements and the reinforcements are embedded lines, both of them governed by a displacements variational formulation. As mentioned for the hand-based yield line method, such non-linear analyses have the interest to provide compatible strains fields at the expense of a stress field strongly in equilibrium and retrieved a posteriori thanks to the constitutive law [dAM17].

To overcome this limitation, a less common choice is to adopt equilibrium approaches, see [dAM17] for a very good review. The history of equilibrium formulation started with the three fields variational principle presented in the concurrent work of Hai-Chang in 1954 [Hc54], Fraeijs de Veubeke in 1965 [FdV65]), and Washizu in 1968 [Was68]. The work of Pian [PT72] was then at the origin of a modified complementary energy principle coupled to an hybrid stress model, which inherits from this three fields variational principle. This extension assumes that equilibrium is imposed to a discontinuous stress field thanks to Lagrange multipliers that can be seen as virtual displacements on tetrahedra faces. More recently the work of Kempeneers [KDB10] and de Almeida and Maunder [dAM17] explored the discretization influences of both stress variables and generalized displacement to lead to accurate dual analysis and error estimation. To sum up, those successive improvements allowed efficient equilibrium elements to emerge, making from now on possible the implementation of numerical static approaches, giving access to stress fields that respect strongly the equilibrium equations.

To our knowledge, the equilibrium approach was investigated for numerical 3D model of reinforced concrete only in ([APO21], [LPN12], [APO22]) and [VABdB18].

In ([APO21], [LPN12], [APO22]), constant stress tetrahedral elements have been used to reduce computation cost. The reinforcements were modeled as smeared reinforcements or discretized explicitly using 3D finite elements. As it will be seen later, this constant stress choice downgrades the equilibrium quality which is one of the reason for the choice of a linear stress field in the present work.

The present work is an alternative approach to the one presented in [VABdB18]. First of all, the problem size has been largely reduced thanks to appropriate discretization choices exposed in 2.3. Then, reinforcements are not smeared anymore since they are modeled as embedded lines. This mixed 1D-3D modelling enables to reduce the high meshing and computation cost of 3D reinforcements and avoids an important loss of information when smearing individual reinforcements into a homogenized region. This choice of reinforcement modeling has been made possible thanks to an innovative variational formulation exposed in 2.1.

Another particularity is the optimization method used to retrieve the solution from the variational formulation. Once the variational formulation is established and the discretization is done, the resulting discrete potential is viewed as the Lagrangian associated with a non-linear mathematical program (see part. 2.2), according to the general method described in [KLSW07]. As shown in [KLSW07], this approach is widely different from the more traditional ones that iterate on displacement increment and compute improved elastoplastic stiffness thanks to the constitutive law. Indeed, this mathematical programming approach offers an unified framework to deal with a wide range of variational formulations and associated discretization, as well as numerous smooth and non smooth yield criteria. For the limit analysis case, it gives access, in the case of perfect plasticity, to upper and lower bounds of a given loading.

Thus, capitalizing on fast and robust methods that recently emerged for convex optimization, we choose to comply with the convex framework developed for dual analysis as exposed in [KLS07], [MM06], and [MM08]. This framework offers a unified approach to dealing with the elastic, elastoplastic, and yield behavior since non-linearity is taken into account only as additional conic constraints. This work is in the continuation of ([EBBA+20b],[EBBA+20a],[VABdB18]), which already stem from the application of convex optimization to deal with frictional contact, Von Mises criterion and Rankine criterion.

Although, a lot of commercial software can be used in order to solve problems complying with the convex optimization framework, the presented work is based on a homemade solver taking advantage of mechanical insight (see part 3.3). Let's add that the formulation has been implemented in a commercial software used for civil engineering studies.At the time being, this commercial software, *Digital Structure*, already dealt with several real-life studies, such as prestressed webs of a reinforced concrete box girder, a prestress anchorage block, a curved and hollowed reinforced concrete wall. This validates the ability of the formulation to cop with the true complexity of non-academic subjects.

The paper is organized as follows. In section 2, the elastic case is discussed with respect to the specific variational formulation (2.1), the discretization(2.3), and the establishment of the discrete Lagrangian needed for the mathematical program (2.2). Section 3 tackles the non-linear extension to the elastoplastic case (3.1) and the particular formulation of limit analysis (3.2). The optimization method and the corresponding interior-point algorithm are exposed in section 3.3. Section 4 deals with three numerical examples that validate the formulation and its numerical implementation. Finally, conclusions are drawn in section 5.

2 The linear elastic case

2.1 The equilibrium variational formulation for reinforced concrete

For a linear elastic material and linear strains, the equilibrium equation system of a 3D mechanical problem, subject to an external surface force $\boldsymbol{t}$, body forces are ignored for simplicity, is written in the following form:

$$\begin{cases} \operatorname{div}\boldsymbol{\sigma} = \mathbf{0}\,, & \text{(1a)} \\ \boldsymbol{\varepsilon} = \nabla^s \boldsymbol{u}\,, & \text{(1b)} \\ \boldsymbol{\sigma} = \boldsymbol{C} : \boldsymbol{\varepsilon}\,, & \text{(1c)} \\ \boldsymbol{\sigma}\,\boldsymbol{n} = \boldsymbol{t} \quad \text{on}\,\Gamma_t\,, & \text{(1d)} \\ \boldsymbol{u} = \bar{\boldsymbol{u}} \quad \text{on}\,\Gamma_u\,, & \text{(1e)} \end{cases}$$

where $\Gamma = \Gamma_u \cup \Gamma_t$ is the closed surface of the solid volume V, $\boldsymbol{C} = 2\mu\boldsymbol{I}_4 + \lambda\boldsymbol{I}_2 \otimes \boldsymbol{I}_2$ is the symmetric fourth-order elasticity tensor, $\boldsymbol{I}_4$ the fourth-order identity tensor, $\boldsymbol{I}_2$ the second order identity tensor, and (μ, λ) are the Lamé coefficients. $\bar{\boldsymbol{u}}$ is the imposed displacement on the Dirichlet boundary Γ_u whereas Γ_t denotes the Neumann boundary where surface tractions $\boldsymbol{t}$ are imposed.

The equation system in (1) represents the equilibrium of the 3D solid i.e., the concrete. Let us now consider a rebar of length L^r and cross-section of area S^r, represented as a 1D line embedded into the concrete. Its geometric position is given by the curve $(\boldsymbol{c}(s)$ where s is the corresponding

curvilinear coordinate. $\boldsymbol{e}^r = \frac{d\boldsymbol{c}(s)}{ds}$ is the corresponding tangent vector. Neglecting the rebar weight, the following additional equations are needed to represent its equilibrium:

$$\begin{cases} \dfrac{d\sigma^r}{ds} = 0\,, & \text{(2a)} \\ \varepsilon^r = \dfrac{du^r}{ds}\,, & \text{(2b)} \\ \sigma^r = E^r \varepsilon^r\,, & \text{(2c)} \\ \sigma^r\, \boldsymbol{e}^r = \boldsymbol{t}^r \quad \text{on } \Gamma_t^r\,, & \text{(2d)} \end{cases}$$

where σ^r is the rebar stress, $u^r = \boldsymbol{u}^r \cdot \boldsymbol{e}^r$ its axial displacement, E^r the Young Modulus, and $\Gamma_t^r = \{0\} \cup \{L^r\}$ the two extremities of the rebar. Finally, an additional bounding constitutive relation should also specify how concrete and rebar displacements are linked together. This point will be discussed again later.

The equation systems in (1) and (2) are generally transformed into a weak form by using the principle of virtual work for a displacement-based formulation. Then, the solution of the problem is numerically approached by discretizing the unknowns over the structure or solid volume.

The displacement and mixed variational formulations are at the basis of the majority of existing finite element models, and therefore they have proven their efficiency in solving various engineering problems. Yet, they have a major drawback: the stress-equilibrium equation in (1a) will not be strongly verified, but only in a weak sense, leading to non-negligible error on the derivation of the stress tensor components.

Since there is no "pure" approach to solve analytically the systems in (1) and (2), another alternative to the classical displacement-based formulation, is to use a stress-based one, by strongly imposing the stress-equilibrium equations in (1a) and (2a). The starting point of this approach is the Hu-Washizu principle, for which we need to express the following functionals:

$$\Pi(\boldsymbol{\sigma}, \boldsymbol{\varepsilon}, \boldsymbol{u}) = \frac{1}{2} \int_V \boldsymbol{\sigma} : \boldsymbol{C}^{-1} : \boldsymbol{\sigma}\, dV + \int_V (\nabla^s \boldsymbol{u} - \boldsymbol{\varepsilon}) : \boldsymbol{\sigma}\, dV - \int_{\Gamma_t} \boldsymbol{t} \cdot \boldsymbol{u}\, d\Gamma\,, \tag{3}$$

$$\Pi^r(\sigma^r, \varepsilon^r, u^r) = \frac{1}{2} \int_{L^r} \frac{\sigma^{r2}}{E^r}\, ds + \int_{L^r} (u^r_{,s} - \varepsilon^r)\sigma^r\, ds - [t^r u^r]_0^{L^r}\,, \tag{4}$$

where $t^r := \boldsymbol{t}^r \cdot \boldsymbol{e}^r$.

Integrating by parts and using the constitutive equation in (1c) and (2c) to eliminate the strains variables form the expression of the functionals, the equations (3) and (4) are transformed into the following forms:

$$\Pi(\boldsymbol{\sigma}, \boldsymbol{u}) = -\frac{1}{2} \int_V \boldsymbol{\sigma} : \boldsymbol{C}^{-1} : \boldsymbol{\sigma}\, dV - \int_V \operatorname{div} \boldsymbol{\sigma} \cdot \boldsymbol{u}\, dV + \int_\Gamma \boldsymbol{\sigma}\, \boldsymbol{n} \cdot \boldsymbol{u}\, d\Gamma - \int_{\Gamma_t} \boldsymbol{t} \cdot \boldsymbol{u}\, d\Gamma\,, \tag{5}$$

$$\Pi^r(\sigma^r, u^r) = -\frac{1}{2} \int_{L^r} \frac{\sigma^{r2}}{E^r}\, ds - \int_{L^r} \sigma^r_{,s}\, u^r\, ds + [(\sigma^r - t^r)u^r]_0^{L^r}\,. \tag{6}$$

Using the stress equilibrium equations $\operatorname{div} \boldsymbol{\sigma} = \boldsymbol{0}$ and $\sigma^r_{,s} = 0$, along with the limit condition (1e), we obtain:

$$\Pi(\boldsymbol{\sigma}, \boldsymbol{u}) = -\frac{1}{2} \int_V \boldsymbol{\sigma} : \boldsymbol{C}^{-1} : \boldsymbol{\sigma}\, dV + \int_{\Gamma_t} (\boldsymbol{\sigma}\, \boldsymbol{n} - \boldsymbol{t}) \cdot \boldsymbol{u}\, d\Gamma + \int_{\Gamma_u} \boldsymbol{\sigma}\, \boldsymbol{n} \cdot \bar{\boldsymbol{u}}\, d\Gamma\,, \tag{7}$$

$$\Pi^r(\sigma^r, u^r) = -\frac{1}{2} \int_{L^r} \frac{\sigma^{r2}}{E^r}\, ds + [(\sigma^r - t^r)u^r]_0^{L^r}\,. \tag{8}$$

The Hu-Washizu principle states that the functionals Π and Π^r must be stationary at the equilibrium state, and therefore leading to the following variational equations:

$$\delta\Pi := \boldsymbol{\nabla}\Pi \cdot \begin{Bmatrix} \delta\boldsymbol{\sigma} \\ \delta\boldsymbol{u} \end{Bmatrix} \Rightarrow \int_V \boldsymbol{\sigma} : \boldsymbol{C}^{-1} : \delta\boldsymbol{\sigma}\, dV - \int_{\Gamma_t} (\boldsymbol{\sigma}\,\boldsymbol{n}\cdot\delta\boldsymbol{u} + \delta\boldsymbol{\sigma}\,\boldsymbol{n}\cdot\boldsymbol{u})\, d\Gamma = \int_{\Gamma_u} \delta\boldsymbol{\sigma}\,\boldsymbol{n}\cdot\bar{\boldsymbol{u}}\, d\Gamma - \int_{\Gamma_t} \boldsymbol{t}\cdot\delta\boldsymbol{u}\, d\Gamma\,, \tag{9}$$

$$\delta\Pi^r := \boldsymbol{\nabla}\Pi^r \cdot \begin{Bmatrix} \delta\sigma^r \\ \delta u^r \end{Bmatrix} \Rightarrow \int_{L^r} \frac{\sigma^r \delta\sigma^r}{E^r}\, ds - [\sigma^r\, \delta u^r + \delta\sigma^r\, u^r]_0^{L^r} = -[t^r\, \delta u^r]_0^{L^r}\,, \tag{10}$$

where $(\delta\boldsymbol{\sigma}, \delta\boldsymbol{u})$ are the concrete virtual symmetric stress tensor and displacement vector respectively, satisfying the equilibrium equation $\operatorname{div}\delta\boldsymbol{\sigma} = \boldsymbol{0}$, and the limit conditions: $\delta\boldsymbol{\sigma}\,\boldsymbol{n} = \boldsymbol{0}$ on Γ_t and $\delta\boldsymbol{u} = \boldsymbol{0}$ on Γ_u. $(\delta\sigma^r, \delta u^r)$ are the rebar virtual stress and displacement components, satisfying the equilibrium equation $\delta\sigma^r_{,s} = 0$, and the limit condition $\delta\sigma^r = 0$ on Γ^r_t.

For what follows, we introduce the Voigt notation, used for a vectorial representation of the stress tensor $\boldsymbol{\sigma}$ as follows:

$$\boldsymbol{\sigma}_v^T = \begin{Bmatrix} \sigma_{xx} & \sigma_{yy} & \sigma_{zz} & \sigma_{xy} & \sigma_{yz} & \sigma_{xz} \end{Bmatrix}\,. \tag{11}$$

This notation is used in the equation (9), so it can be re-written as follows:

$$\int_V \boldsymbol{\sigma}_v^T \boldsymbol{C}_v^{-1} \delta\boldsymbol{\sigma}_v\, dV - \int_{\Gamma_t} (\boldsymbol{P}\boldsymbol{\sigma}_v \cdot \delta\boldsymbol{u} + \boldsymbol{P}\delta\boldsymbol{\sigma}_v \cdot \boldsymbol{u})\, d\Gamma = \int_{\Gamma_u} \boldsymbol{P}\delta\boldsymbol{\sigma}_v \cdot \bar{\boldsymbol{u}}\, d\Gamma - \int_{\Gamma_t} \boldsymbol{t}\cdot\delta\boldsymbol{u}\, d\Gamma\,, \tag{12}$$

where:

$$\boldsymbol{P} := \begin{bmatrix} n_x & 0 & 0 & n_y & n_z & 0 \\ 0 & n_y & 0 & n_x & 0 & n_z \\ 0 & 0 & n_z & 0 & n_x & n_y \end{bmatrix}\,, \tag{13}$$

and $\boldsymbol{C}_v$ is the corresponding 6×6 matrix of elastic moduli.

At this stage, to be able to solve the integral equation in (12), the domain V is discretized with the aid of 3D finite elements, where the stress components are interpolated over V (see section 2.3 for more details), whereas the displacement components are only interpolated over the external contour Γ_t. Nevertheless, to impose for the interpolated stresses to be continuous and to strongly satisfy $\operatorname{div}\delta\boldsymbol{\sigma} = \boldsymbol{0}$ over V, they need to be at least differentiable of class C^1 (see [FdV65]), a condition very difficult to ensure for a three-dimensional interpolation. Indeed, for a tetrahedral discretization, the interpolation needs to be a polynomial of degree 9 or higher (see [Zha09]), in order to be C^1 over the entire domain.

Instead of using a C^1 interpolation over V, we will consider in this work a piece-wise interpolation for the stress components [Kem06, MM08]. The condition $\operatorname{div}\delta\boldsymbol{\sigma} = \boldsymbol{0}$ can then be easily enforced for each element, while allowing statically admissible discontinuities at the interfaces between elements. For this approach, as it will be shown, the displacement vector will be needed at the triangular (or quadrilateral) faces of the mesh, and not only at the external contour Γ of the volume V.

To develop this approach, let us first recast the corresponding equations in the form of a minimization problem, where the coupling between the concrete and the rebar stresses will be introduced.

2.2 Optimization form of the equilibrium-based formulation:

First, let us recall that the equilibrium formulation for reinforced concrete can be equivalently cast in the form of an optimization problem, expressed as follows:

$$\begin{cases} \min\limits_{(\boldsymbol{\sigma},\sigma^r)\in SA} \psi(\boldsymbol{\sigma},\sigma^r) - \displaystyle\int_{\Gamma_u} \boldsymbol{\sigma n}\cdot\bar{\boldsymbol{u}}\, d\Gamma\,, & \text{(14a)} \\ \text{s.t.} \quad \boldsymbol{\sigma}\,\boldsymbol{n} = \boldsymbol{t} \quad \text{on } \Gamma_t\,, & \text{(14b)} \\ \sigma^r = t^r \quad \text{on } \Gamma_t^r\,, & \text{(14c)} \end{cases}$$

where:

$$\psi(\boldsymbol{\sigma},\sigma^r) := \frac{1}{2}\int_V \boldsymbol{\sigma} : \boldsymbol{C}^{-1} : \boldsymbol{\sigma}\, dV + \frac{S^r}{2}\int_{L^r} \frac{{\sigma^r}^2}{E^r}\, ds\,, \tag{15}$$

is the complementary energy, and $(\boldsymbol{\sigma},\sigma^r) \in SA$ means that the stress fields are statically admissible stresses i.e., they satisfy the equilibrium equations (1a) and (2a).

To illustrate the equivalence between the optimization problem above and the integral equations in (9) and (10), we start by writing the Lagrangian of problem (14):

$$\mathcal{L}(\boldsymbol{\sigma},\sigma^r,\boldsymbol{u},u^r) = \psi(\boldsymbol{\sigma},\sigma^r) - \int_{\Gamma_t} (\boldsymbol{\sigma}\,\boldsymbol{n}-\boldsymbol{t})\cdot\boldsymbol{u}\, d\Gamma - \int_{\Gamma_u} \boldsymbol{\sigma}\,\boldsymbol{n}\cdot\bar{\boldsymbol{u}}\, d\Gamma - S^r[\,(\sigma^r - t^r)u^r\,]_0^{L^r}\,, \tag{16}$$

where we used the integral form of the constraints in (14b) and (14c), for which $(\boldsymbol{u},u^r)$ can be interpreted here as their associated Lagrange multipliers. Note that, at this stage, the latter are defined on Γ_t and Γ_u only.

From the expression of the Lagrangian above, the following relation is directly obtained:

$$\mathcal{L}(\boldsymbol{\sigma},\sigma^r,\boldsymbol{u},u^r) = -(\,\Pi(\boldsymbol{\sigma},\boldsymbol{u}) + S^r\Pi^r(\sigma^r,u^r)\,)\,, \tag{17}$$

and thus, the optimality conditions for the optimization problem (14) are expressed as follows:

$$\boldsymbol{\nabla}\mathcal{L}\cdot\begin{Bmatrix}\delta\boldsymbol{\sigma}\\ \delta\boldsymbol{u}\end{Bmatrix} = -\delta\Pi = 0\,, \tag{18}$$

$$\boldsymbol{\nabla}\mathcal{L}\cdot\begin{Bmatrix}\delta\sigma^r\\ \delta u^r\end{Bmatrix} = -\delta\Pi^r = 0\,, \tag{19}$$

for any statically admissible stress variation $(\delta\boldsymbol{\sigma},\delta\sigma^r) \in SA$ and any boundary displacement variation $(\delta\boldsymbol{u},\delta u^r)$. This proves the equivalence between the optimization problem in (14) and the equations in (9) and (10), deduced from the Hu-Washizu principle.

Now, to find a numerical solution of (14), we suppose that the volume is discretized into n_{vol} finite-elements V_i over which a specific discretization of the stress field will be later chosen. As regards the rebars, they will be discretized into segments corresponding to the intersection with the triangular faces of the mesh (see Fig.1):

$$L^r = \Delta L_1^r \cup \Delta L_2^r \cup \cdots \cup \Delta L_{n_{rebar}}^r\,, \tag{20}$$

where $\Delta L_i^r = s_{i+1} - s_i$, $I^r = \{s_i \quad | \quad i \in [\![1, n_{rebar}+1]\!]\}$ the abscissas of the rebar intersecting the mesh, and n_{rebar} the total number of 1D elements discretizing the length of the rebar.

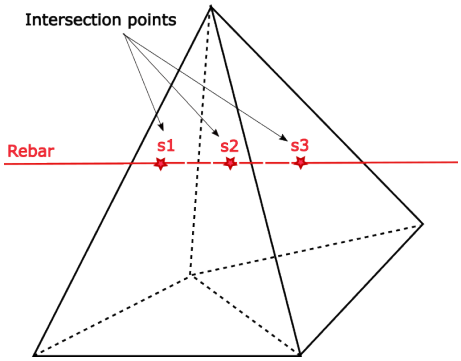

Figure 1: Intersection points between mesh triangular faces of two tetrahedra and a rebar.

The discretized form of the functional (15) is then expressed as follows:

$$\psi(\boldsymbol{\sigma}, \sigma^r) = \frac{1}{2} \sum_{i=1}^{n_{vol}} \int_{V_i} \boldsymbol{\sigma}_i : \boldsymbol{C}^{-1} : \boldsymbol{\sigma}_i \, dV + \frac{1}{2} \sum_{i=1}^{n_{rebar}} \int_{\Delta L_i^r} \frac{S^r \sigma_i^{r\,2}}{E^r} \, ds \,, \tag{21}$$

where $\boldsymbol{\sigma}_i$ is the stress field inside the ith tetrahedral element, and σ_i^r is the rebar stress inside the ith portion of the rebar.

As explained in 2.1, when a piece-wise interpolation is considered, additional constraints are necessary to assure statically admissible discontinuities on the interpolated stress. More precisely, through any interface Δ_i between two adjacent elements (see Fig.2), the concrete traction vector must be continuous i.e. $[\![\boldsymbol{\sigma}]\!]\boldsymbol{n} = (\boldsymbol{\sigma}_2 - \boldsymbol{\sigma}_1)\boldsymbol{n} = \boldsymbol{0}$. Similarly, the rebar stress must also be continuous at points $s_j \in I_r$ crossing an arbitrary interface Δ_i i.e. $[\![\sigma^r]\!] = \sigma_2^r - \sigma_1^r = 0$.

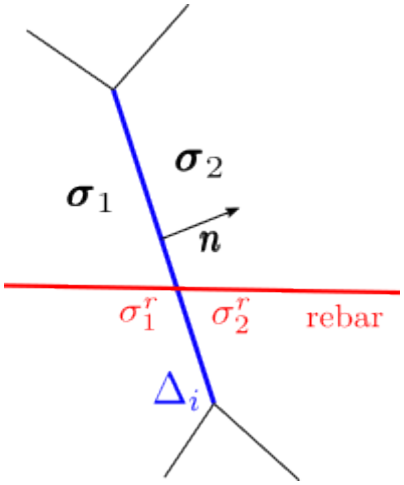

Figure 2: A rebar intersecting an interface Δ_i.

Thus, the discretized form of the constrained optimization problem in (14) is expressed as follows:

$$\begin{cases} \min\limits_{(\boldsymbol{\sigma},\sigma^r)\in SA_b} \psi(\boldsymbol{\sigma}, \sigma^r) - \displaystyle\int_{\Gamma_u} \boldsymbol{\sigma}\boldsymbol{n} \cdot \bar{\boldsymbol{u}} \, d\Gamma \,, & \text{(22a)} \\ \quad \text{s.t.} \quad \boldsymbol{\sigma}\,\boldsymbol{n} = \boldsymbol{t} \quad \text{on } \Gamma_t \,, & \text{(22b)} \\ \qquad \sigma^r = t^r \quad \text{on } \Gamma_t^r \,, & \text{(22c)} \\ \qquad [\![\boldsymbol{\sigma}]\!]\boldsymbol{n} = 0 \quad \text{on all } \Delta_i \,, & \text{(22d)} \\ \qquad [\![\sigma^r]\!] = 0 \quad \text{on all } s_j \in I^r \,, & \text{(22e)} \end{cases}$$

where $(\boldsymbol{\sigma}, \sigma^r) \in SA_b$ means that $\operatorname{div} \boldsymbol{\sigma} = \mathbf{0}$ for each finite volume V_i, and $\sigma^r_{,s} = 0$ for each rebar portion ΔL^r_i.

When forming the Lagrangian of the previous system, additional Lagrange multipliers appear with respect to the last two continuity conditions. Such multipliers can be interpreted as displacement fields $\boldsymbol{u}$ (resp. u^r) which are now defined over all external faces Γ_t and internal faces $\bigcup_i \Delta_i$ (resp. external extremities Γ^r_t and internal intersection points I_r).

At this stage, the coupling between the concrete variables $(\boldsymbol{\sigma}, \boldsymbol{u})$ and the rebars' (σ^r, u^r) have not yet been introduced. In the following, we will make a *perfect bonding hypothesis* between the rebars and the concrete. More precisely, we posit that both displacements coincide on the rebar i.e. $u_r(s_i) = \boldsymbol{e}^r \cdot \boldsymbol{u}(s_i)$. Inspecting the corresponding Lagrangian, one can see that such an assumption can be interpreted as enforcing the continuity of an effective traction vector merging the contribution of both the concrete and the rebar stress, rather than asking for a continuity of both stresses separately.

2.3 The finite-element formulation

We now discuss the corresponding finite-element formulation by choosing a specific interpolation for the unknown fields. We consider in the following that the concrete stress field varies linearly inside each tetrahedral finite element. As previously stated, the stress components are not continuous over V since they are independently interpolated over each element, while assuring statically admissible discontinuities over the faces of the tetrahedra through the Lagrange multiplier $\boldsymbol{u}$. Thus, each tetrahedral finite element has 24 independent stress degrees of freedom. For the displacement components $\boldsymbol{u}$, they are also interpolated linearly over the faces of the mesh, making 9 displacement degrees of freedom per triangular face (see Fig. 3). The choice of a linear interpolation over the faces for the displacements components is not arbitrary. Indeed, in the absence of any reinforcement, a linear $\boldsymbol{u}$ on each face is enough to enforce strongly the traction continuity of the concrete stress since the latter is also linear on a face.

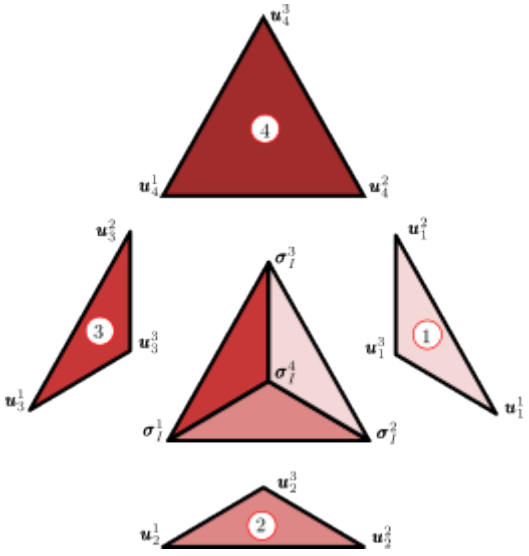

Figure 3: Stress and displacement degrees of freedom of a linear tetrahedron.

For each portion between two intersection points, the rebar stress is constant ($\sigma^r_{,s} = 0$) and thus it is associated with only one degree of freedom. Consequently, σ^r is piece-wise constant over the total length L^r of the rebar.

Thus, for the equilibrium-based finite element formulation, the total number of degrees of freedom is computed with the following formula:

$$n_{dof} = 24 \times n_{vol} + 9 \times n_{face} + n_{rebar}\,, \tag{23}$$

where n_{dof} is the total number of degrees of freedom, n_{vol} the number of tetrahedral finite elements, and n_{face} the number of triangular faces of the meshing.

For an arbitrary linear tetrahedral element V_0, the interpolation of the six stress components over the volume's element, and that of the three displacement components over the closed surface Γ_0, formed with the four triangular faces of the tetrahedra will be noted as follows:

$$\boldsymbol{\sigma}_v = \boldsymbol{N}_\sigma \, \tilde{\boldsymbol{\sigma}} \quad , \quad \boldsymbol{u} = \boldsymbol{N}_u \, \tilde{\boldsymbol{u}} \, , \tag{24}$$

where $\boldsymbol{N}_\sigma$ and $\boldsymbol{N}_u$ contain the interpolation functions of the stress and displacement components respectively, $\tilde{\boldsymbol{\sigma}}$ is the stress degrees of freedom vector of dimension 24 (6 per vertex), and $\tilde{\boldsymbol{u}}$ is the displacement degrees of freedom vector of dimension 36 (9 per triangular face).

For the rebar's displacement u^r, it is needed only at the intersection points $\boldsymbol{p}_1$ and $\boldsymbol{p}_2$ with Γ_0, at the abscissas s_1 and s_2 of the rebar, and therefore, it will be linked to the displacement of the intersected triangular face using the following relation:

$$u_r(s_\alpha) = \boldsymbol{e}^r \cdot \boldsymbol{u}(\boldsymbol{p}_\alpha) \quad \Rightarrow \quad u_r(s_\alpha) = \boldsymbol{N}_u^r(s_\alpha) \, \tilde{\boldsymbol{u}} \, , \tag{25}$$

where $\boldsymbol{N}_u^r(s_\alpha) = \boldsymbol{e}^{r\,T} \boldsymbol{N}_u(\boldsymbol{p}_\alpha)$ and α equal to 1 or 2 for the two extremities of the rebar portion.

Moreover, we recall that the stress tensor $\boldsymbol{\sigma}$ of the concrete must satisfy the equilibrium equations $\operatorname{div} \boldsymbol{\sigma} = \boldsymbol{0}$. These are additional constraints that can be easily imposed by using new Lagrange multipliers, or by reducing the number of tetrahedral stress degrees of freedom from 24 to 21 using an appropriate choice of shape functions, see [KDB10, Kem06] for more details. In this case, the total number of degrees of freedom becomes:

$$n_{dof} = 21 \times n_{vol} + 9 \times n_{face} + n_{rebar} \, . \tag{26}$$

Note that in presence of a non-zero body force $\boldsymbol{b}$, a particular solution $\boldsymbol{\sigma}_b$ to the equation $\operatorname{div} \boldsymbol{\sigma} = \boldsymbol{b}$ should be found and added to the previous stress unknowns. See [Kem06] for more details.

Let us now discuss the construction of the corresponding elementary stiffness/flexibility matrix for an arbitrary element V_0. For simplicity, we assume that its closed contour Γ_0 does not intersect the exterior boundary. The contribution of this element to the system Lagrangian reads:

$$\mathcal{L}_0 = \frac{1}{2} \int_{V_0} \boldsymbol{\sigma}_v^T \boldsymbol{C}_v^{-1} \boldsymbol{\sigma}_v \, dV + \int_{\Gamma_0} \boldsymbol{P} [\![\boldsymbol{\sigma}_v]\!] \cdot \boldsymbol{u} \, d\Gamma + \frac{S^r}{2} \int_{\Delta L^r} \frac{(\sigma^r)^2}{E^r} \, ds + S^r [\![\sigma^r]\!] u_r]_{s_1}^{s_2} \, . \tag{27}$$

Using the relations (24) and (25), the variation of this contribution with respect to the concrete stress degrees of freedom $\tilde{\boldsymbol{\sigma}}$ yields the corresponding equilibrium of element V_0:

$$\delta\tilde{\boldsymbol{\sigma}} \left(\int_{V_0} \boldsymbol{N}_\sigma^T \boldsymbol{C}_v^{-1} \boldsymbol{N}_\sigma \, dV \right) \tilde{\boldsymbol{\sigma}} - \delta\tilde{\boldsymbol{\sigma}} \left(\int_{\Gamma_0} \boldsymbol{N}_\sigma^T \boldsymbol{P}^T \boldsymbol{N}_u \, d\Gamma \right) \tilde{\boldsymbol{u}} = 0 \quad \forall \delta\tilde{\boldsymbol{\sigma}} \, , \tag{28}$$

which yields the following matrix equation:

$$\boldsymbol{F} \tilde{\boldsymbol{\sigma}} - \boldsymbol{H} \tilde{\boldsymbol{u}} = 0 \, , \tag{29}$$

with

$$\boldsymbol{F} = \int_{V_0} \boldsymbol{N}_\sigma^T \, \boldsymbol{C}_v^{-1} \, \boldsymbol{N}_\sigma \, dV, \quad \boldsymbol{H} = \int_{\Gamma_0} \boldsymbol{N}_\sigma^T \, \boldsymbol{P}^T \, \boldsymbol{N}_u \, d\Gamma \, . \tag{30}$$

Similarly, the variation of (27) with respect to the rebar stress yields:

$$\delta\sigma^r \frac{S^r \Delta L^r}{E^r}\sigma^r - \delta\sigma^r S^r(\boldsymbol{N}_u^r(s_2) - \boldsymbol{N}_u^r(s_1))\tilde{\boldsymbol{u}} = 0\,. \tag{31}$$

Introducing $\boldsymbol{H}^r = S^r(\boldsymbol{N}_u^r(s_2) - \boldsymbol{N}_u^r(s_1))$, we have for element V_0:

$$\begin{bmatrix} \frac{\Delta L^r S^r}{E^r} & \mathbf{0} & -\boldsymbol{H}^r \\ \mathbf{0} & \boldsymbol{F} & -\boldsymbol{H} \end{bmatrix} \begin{Bmatrix} \tilde{\sigma}^r \\ \tilde{\boldsymbol{\sigma}} \\ \tilde{\boldsymbol{u}} \end{Bmatrix} = \begin{Bmatrix} 0 \\ 0 \end{Bmatrix}. \tag{32}$$

Finally, the variation of (27) with respect to the displacement dofs yields the traction continuity equilibrium equation which links the internal stress state inside V_0 with the stress dofs $\tilde{\boldsymbol{\sigma}}_{adj}$ and σ^r_{adj} of the adjacent elements. Formally, this continuity equation can be written as:

$$-\boldsymbol{H}^T\tilde{\boldsymbol{\sigma}} - (\boldsymbol{H}^r)^T\sigma^r + (\boldsymbol{H}_{adj})^T\tilde{\boldsymbol{\sigma}}_{adj} + (\boldsymbol{H}^r_{adj})^T\sigma^r_{adj} = \mathbf{0}\,. \tag{33}$$

Note that when V_0 shares a face with Γ_t, one has to include the contribution of the imposed traction vector, resulting in a non-zero right-hand side.

One key property of hybrid mixed methods is that stress variables, namely $\tilde{\sigma}^r$ and $\tilde{\boldsymbol{\sigma}}$ are local to the considered element. These two equations can therefore be reduced by static condensation of the stress variables inside each element, yielding:

$$\begin{Bmatrix} \tilde{\sigma}^r \\ \tilde{\boldsymbol{\sigma}} \end{Bmatrix} = \bar{\boldsymbol{F}}^{-1}\bar{\boldsymbol{H}}\tilde{\boldsymbol{u}}\,, \tag{34}$$

where:

$$\bar{\boldsymbol{H}} = \begin{bmatrix} \boldsymbol{H}^r \\ \boldsymbol{H} \end{bmatrix}, \quad \bar{\boldsymbol{F}} = \begin{bmatrix} \frac{\Delta L^r S^r}{E^r} & \mathbf{0} \\ \mathbf{0} & \boldsymbol{F} \end{bmatrix}. \tag{35}$$

Injecting this relation into the elementary Lagrangian (27), the resulting system will involve only displacement variables which are shared by neighbour elements. The resulting elementary stiffness matrix of element V_0 will then be given by:

$$\boldsymbol{K} = \bar{\boldsymbol{H}}^T\bar{\boldsymbol{F}}^{-1}\bar{\boldsymbol{H}}\,, \tag{36}$$

We note that $\bar{\boldsymbol{F}}$ is a 25×25 symmetric positive definite matrix, and thus the stiffness matrix $\boldsymbol{K}$ is also a symmetric 36×36 matrix of rank lesser or equal to 25. It implies that $\boldsymbol{K}$ has at least 11 zero eigenvalue modes, instead of only 6 for the classical rigid-body modes. The origin of these spurious modes is very well documented in [KDB10, Kem06, dAM17, MdAR96], and there are different approaches to eliminate them. An efficient and simple method consists in subdividing each tetrahedral element into four sub-elements by adding a node in the barycentric center. Hence, a super element is formed by assembling the four sub-tetrahedra that will be construction-free from any spurious modes.

By introducing the following notations for $\boldsymbol{q}$, the vector of dimension $n_{stress} = 24 \times n_{vol} + n_{rebar}$ containing all the stress degrees of freedom of the system, and $\boldsymbol{A}$, the global (flexibility) matrix assembled from the tetrahedra elementary matrices:

$$\boldsymbol{q}^T = \begin{Bmatrix} \sigma^r_1 & \cdots & \sigma^r_{n_{rebar}} & \boldsymbol{\sigma}_1 & \cdots & \boldsymbol{\sigma}_{n_{vol}} \end{Bmatrix}, \tag{37}$$

$$\boldsymbol{A} = \begin{bmatrix} \frac{\Delta L_1^r S^r}{E^r} & & & & \mathbf{0} \\ & \ddots & & & \\ & & \frac{\Delta L_{n_{rebar}}^r S^r}{E^r} & & \\ & & & \boldsymbol{F}_1 & \\ & & & & \ddots \\ \mathbf{0} & & & & \boldsymbol{F}_{n_{vol}} \end{bmatrix}, \tag{38}$$

the optimization problem in (22) can be expressed in a matrix form as follows:

$$\begin{cases} \min\limits_{\boldsymbol{q} \in \mathbb{R}^{n_{stress}}} \left(\frac{1}{2} \boldsymbol{q}^T \boldsymbol{A}\, \boldsymbol{q} - \boldsymbol{c}_u^T \boldsymbol{q} \right), & \text{(39a)} \\ \quad \text{s.t.} \quad \widehat{\boldsymbol{H}} \boldsymbol{q} = \boldsymbol{c}_t\,, & \text{(39b)} \end{cases}$$

where $\boldsymbol{c}_u$ is the imposed displacement loading vector assembled from the corresponding objective function in (22a), $\widehat{\boldsymbol{H}}$ corresponds to the global matrix assembled from (33) and $\boldsymbol{c}_t$ is the associated right-hand side corresponding to the external tractions applied on Γ_t.

3 The non-linear case

3.1 Elastoplastic analysis

In this work, we benefit from the use of efficient optimization algorithms to formulate an elastoplastic analysis of the equilibrium-based formulation through a convex minimization principle. Rather than relying on standard strain-driven implementations of plasticity using return mapping algorithms, the proposed formulation enables to consider non-smooth yield surfaces (including apexes or multi-surface plasticity) without any additional difficulty. It is indeed known that non-smooth yield surfaces present numerical difficulties in the context of return mapping algorithms. The main requirement is that the yield surface should be expressed through simple convex constraints involving for instance second-order cones or the cone of semi-definite matrices. Fortunately, most of the usual yield criteria can be expressed in such a format, see for instance [BP07, Mak10]. Another interest in formulating elastoplastic problems in the framework of convex optimization is that it can be easily adapted to limit analysis formulations, in which the limit load of a perfectly elastoplastic structure is computed directly, in a single convex optimization resolution, without relying on a step-by-step analysis up to collapse. This will be the purpose of section 3.2.

Elastoplastic behaviour entails a path-dependent response of the underlying boundary-value problem. In theory, the path-dependent solution should be obtained by integrating over a loading path the material constitutive behaviour written in terms of stress and strain rates. In practice however, a finite-step time discretization is used and rates are approximated with finite increments. Over such increments, the finite-step evolution is equivalent to a holonomic plasticity formulation which is a reasonable approximation for radial load paths. Convergence to the real path-dependent solution is then obtained for sufficient time step discretization, especially when the loading path deviates from a radial load path. Here, we consider only a monotonous radial load path for simplicity. In this case, a single step holonomic provides a very good estimate of the true solution [GRM88]. This enables in particular to compute the plastic collapse state in a single computation, akin to limit analysis formulations. Obviously, in the general case, one should resort to an incremental formulation of plasticity, as done for instance in [KLS07, KLSW07, EBBA+20b], which would require only minor modifications to the following formulation. Similarly, hardening can also be consider in the same framework.

The single-step elastoplastic formulation is obtained here by simply introducing plastic yield conditions as additional constraints into the minimization problem in (14), with respect to the concrete and rebar stress components, as follows:

$$\begin{cases} \min\limits_{(\boldsymbol{\sigma},\sigma^r)\in SA} \psi(\boldsymbol{\sigma},\sigma^r) - \displaystyle\int_{\Gamma_u} \boldsymbol{\sigma}\boldsymbol{n}\cdot\bar{\boldsymbol{u}}\, d\Gamma\,, & \text{(40a)} \\ \text{s.t.} \quad \boldsymbol{\sigma}\,\boldsymbol{n} = \boldsymbol{t} \quad \text{on } \Gamma_t\,, & \text{(40b)} \\ \qquad \sigma^r = t^r \quad \text{on } \Gamma_t^r\,, & \text{(40c)} \\ \qquad f(\boldsymbol{\sigma}) \le 0 \quad \text{on } V\,, & \text{(40d)} \\ \qquad |\sigma^r| \le f_y \quad \text{on } L^r\,, & \text{(40e)} \end{cases}$$

where the function $f(\boldsymbol{\sigma})$ represents here the concrete yield criterion and f_y is the elastic limit of the rebars.

Next, we detail two criteria which to model the yield condition for concrete: the truncated Mohr-Coulomb (TMC):

$$\begin{cases} K\sigma_I - \sigma_{III} - f_c \le 0\,, & \text{(41a)} \\ \sigma_I - f_t \le 0\,, & \text{(41b)} \end{cases}$$

and the Rankine (Ra) yield criterion:

$$\begin{cases} -\sigma_{III} - f_c \le 0\,, & \text{(42a)} \\ \sigma_I - f_t \le 0\,, & \text{(42b)} \end{cases}$$

where σ_I and σ_{III} are, respectively, the maximum and minimum principal values of the stress tensor $\boldsymbol{\sigma}$, f_c the compression limit of the concrete, f_t its tensile limit, and $K := (1+\sin\phi)/(1-\sin\phi)$ a material constant depending on the friction angle ϕ.

We note that the difference between the classical Mohr-Coulomb criterion and the truncated one, is the additional constraint in (41b), limiting the tensile strength of the material to a value f_t (near zero for the concrete). This additional condition is necessary for a more realistic characterization of the concrete behavior.

Since the constraints in (41) and (42) are expressed in terms of the principal values of the stress tensor, the optimization problem in (40) falls into the category of semidefinite programming (SDP), where the non-linear constraints are expressed in the form of matrices that are subjected to be positive (or negative) semidefinite. Thus, the constraints in (41) and (42) are reformulated into the following equivalent forms:

$$\begin{cases} \boldsymbol{\sigma} - x\boldsymbol{I} \preceq \boldsymbol{0}\,, & \text{(43a)} \\ -\boldsymbol{\sigma} + Kx\boldsymbol{I} - f_c\boldsymbol{I} \preceq \boldsymbol{0}\,, & \text{(43b)} \\ x \le f_t\,, & \text{(43c)} \end{cases}$$

and:

$$\begin{cases} -\boldsymbol{\sigma} - f_c\boldsymbol{I} \preceq \boldsymbol{0}\,, & \text{(44a)} \\ \boldsymbol{\sigma} - f_t\boldsymbol{I} \preceq \boldsymbol{0}\,, & \text{(44b)} \end{cases}$$

where $\cdot \preceq \boldsymbol{0} (\cdot \succeq \boldsymbol{0})$ denotes a negative (positive) semi-definite matrix, and x is an additional slack variable, introduced to be able to express the constraints in (41) in a format suitable for the SDP optimization framework [MM08, LPN12].

The SDP constraints in (43) or (44) are imposed at each one of the four vertices of the linear tetrahedra. Thus, the total number of constraints for each criterion is equal to:

$$n_{MCT} = 12 \times n_{vol}, \quad n_{RA} = 8 \times n_{vol}\,, \tag{45}$$

where n_{MCT} and n_{Ra} are the number of constraints for the truncated Mohr-Coulomb and Rankine criterions, respectively.

For the Rankine criterion, we write the final discretized form of the optimization problem (40), representing the elastoplastic equilibrium-based formulation for reinforced concrete:

$$\begin{cases} \min\limits_{\boldsymbol{q}\in\mathbb{R}^{n_{stress}}} \left(\frac{1}{2}\boldsymbol{q}^T\boldsymbol{A}\,\boldsymbol{q} - \boldsymbol{c}_u^T\boldsymbol{q}\right), & \text{(46a)} \\ \quad \text{s.t. } \widehat{\boldsymbol{H}}\boldsymbol{q} = \boldsymbol{c}_t & \text{(46b)} \\ \quad\quad \forall i \in [\![1, n_{vol}]\!],\ \forall k \in [\![1,4]\!],\ -\boldsymbol{\sigma}_i(k) - f_c\boldsymbol{I} \preceq \boldsymbol{0}, & \text{(46c)} \\ \quad\quad \forall i \in [\![1, n_{vol}]\!],\ \forall k \in [\![1,4]\!],\ \boldsymbol{\sigma}_i(k) - f_t\boldsymbol{I} \preceq \boldsymbol{0}, & \text{(46d)} \\ \quad\quad \forall i \in [\![1, n_{rebar}]\!],\ |\sigma_i^r| \leq f_y, & \text{(46e)} \end{cases}$$

where $\boldsymbol{\sigma}_i(k)$ represents the stress tensor degrees of freedom of the kth vertex of the ith element.

Clearly, the existence of a solution for the problem above is not always assured since it is loading and material dependent. It allows us to introduce the important concept of the limit load, detailed in the next section.

3.2 Limit analysis and the lower bound of the collapse load

For a given load direction denoted by $(F)_{ext}$, the lower bound limit analysis approach is used to directly obtain the maximum multiplicative factor λ, for which $\lambda(F)_{ext}$ can no longer be equilibrated by the structure. It supposes a rigid-plastic behavior of the structure, where the elastic phase is neglected. Thus, this approach can only be applied to sufficiently ductile structures, for which the coefficient λ can be interpreted as a security factor associated to $(F)_{ext}$, and $\lambda(F)_{ext}$ is a limit load.

Limit analysis has many applications in civil engineering and is widely used for the safety evaluation of steel assemblies (see [EBBA+20b, EBBA+20a]), concrete structures, and geotechnical works. Compared to the incremental approach, where the external loading is increased step by step until the numerical solution diverge, the limit analysis approach will directly calculate the limit load in one increment. It is also naturally adapted to the optimization framework, since we are looking to maximize the load factor λ in a given load direction, expressed in terms of $\boldsymbol{t}$ and t^r (here we assume $\bar{\boldsymbol{u}} = 0$).

The lower bound limit analysis problem is expressed in the following form:

$$\begin{cases} \max\limits_{(\boldsymbol{\sigma},\sigma^r)\in SA} \lambda, & \text{(47a)} \\ \quad \text{s.t. } \boldsymbol{\sigma}\,\boldsymbol{n} = \lambda\boldsymbol{t} \quad \text{on } \Gamma_t, & \text{(47b)} \\ \quad\quad \sigma^r = \lambda t^r \quad \text{on } \Gamma_t^r, & \text{(47c)} \\ \quad\quad f(\boldsymbol{\sigma}) \leq 0 \quad \text{on } V, & \text{(47d)} \\ \quad\quad |\sigma^r| \leq f_y \quad \text{on } L^r, & \text{(47e)} \end{cases}$$

For a given mesh, the optimization problem above is reformulated into the following equivalent minimization problem:

$$
\begin{cases}
\min\limits_{(\boldsymbol{\sigma},\sigma^r)\in SA_b} -\lambda, & (48a)\\
\quad \text{s.t.} \quad \boldsymbol{\sigma}\,\boldsymbol{n} = \lambda \boldsymbol{t} \quad \text{on } \Gamma_t\,, & (48b)\\
\qquad \sigma^r = \lambda t^r \quad \text{on } \Gamma_t^r\,, & (48c)\\
\qquad [\![\boldsymbol{\sigma}]\!]\boldsymbol{n} = 0 \quad \text{on all } \Delta_i\,, & (48d)\\
\qquad [\![\sigma^r]\!] = 0 \quad \text{on all } s_j \in I^r\,, & (48e)\\
\qquad \forall i \in [\![1, n_{vol}]\!],\ \forall k \in [\![1,4]\!],\ -\boldsymbol{\sigma}_i(k) - f_c \boldsymbol{I} \preceq \boldsymbol{0}\,, & (48f)\\
\qquad \forall i \in [\![1, n_{vol}]\!],\ \forall k \in [\![1,4]\!],\ \boldsymbol{\sigma}_i(k) - f_t \boldsymbol{I} \preceq \boldsymbol{0}\,, & (48g)\\
\qquad \forall i \in [\![1, n_{rebar}]\!],\ |\sigma_i^r| \leq f_y\,, & (48h)
\end{cases}
$$

and by using the following notations:

$$
\boldsymbol{q}_\lambda = \begin{Bmatrix} \boldsymbol{q} \\ \lambda \end{Bmatrix}\,, \quad \widehat{\boldsymbol{H}}_\lambda = \begin{bmatrix} \hat{\boldsymbol{H}} & -\boldsymbol{c}_t \end{bmatrix}\,, \quad \boldsymbol{c}_\lambda = \begin{Bmatrix} \boldsymbol{0} \\ 1 \end{Bmatrix}\,. \tag{49}
$$

the optimization problem is expressed in the following final matrix form :

$$
\begin{cases}
\min\limits_{\boldsymbol{q}_\lambda \in \mathbb{R}^{1+n_{stress}}} -\boldsymbol{c}_\lambda^T \boldsymbol{q}_\lambda\,, & (50a)\\
\quad \text{s.t.}\ \widehat{\boldsymbol{H}}_\lambda \boldsymbol{q}_\lambda = \boldsymbol{0} & (50b)\\
\qquad \forall i \in [\![1, n_{vol}]\!],\ \forall k \in [\![1,4]\!],\ -\boldsymbol{\sigma}_i(k) - f_c \boldsymbol{I} \preceq \boldsymbol{0}\,, & (50c)\\
\qquad \forall i \in [\![1, n_{vol}]\!],\ \forall k \in [\![1,4]\!],\ \boldsymbol{\sigma}_i(k) - f_t \boldsymbol{I} \preceq \boldsymbol{0}\,, & (50d)\\
\qquad \forall i \in [\![1, n_{rebar}]\!],\ |\sigma_i^r| \leq f_y\,, & (50e)
\end{cases}
$$

For limit analysis, the total number of degrees of freedom is equal to $n_\lambda = n_{dof} + 1$, where we recall that n_{dof} is the number of degrees of freedom for the elastic and elastoplastic cases.

3.3 Cone programming solver

The optimization problems resulting from the equilibrium finite-element discretization of either the elastoplastic or limit analysis formulation can be cast into the following generic *quadratic cone programming form*:

$$
\begin{array}{ll}
\min\limits_{\boldsymbol{x},\boldsymbol{s}} & \frac{1}{2}\boldsymbol{x}^T \boldsymbol{P} \boldsymbol{x} + \boldsymbol{c}^T \boldsymbol{x} \\
\text{s.t.} & \boldsymbol{A}\boldsymbol{x} = \boldsymbol{b} \\
& \boldsymbol{G}\boldsymbol{x} + \boldsymbol{s} = \boldsymbol{h} \\
& \boldsymbol{s} \in \mathcal{K}
\end{array} \tag{51}
$$

where $\boldsymbol{x}$ are the main optimization variables (here $\boldsymbol{q}$ or $\boldsymbol{q}$ and λ) and $\boldsymbol{s}$ are conic slack variables which must belong to a cone $\mathcal{K}$ which is supposed to be given by a Cartesian product of smaller cones i.e.:

$$
\mathcal{K} = \mathcal{K}_1 \times \ldots \times \mathcal{K}_K \tag{52}
$$

where each $\mathcal{K}_i$ can be one of the following elementary cones:

- the positive orthant:

$$
\mathcal{K}_i = \{\boldsymbol{y} \text{ s.t. } y_j \geq 0\} \tag{53}
$$

- the Lorentz second-order cone:

$$
\mathcal{K}_i = \{\boldsymbol{y} = (y_0, \bar{\boldsymbol{y}}) \text{ s.t. } \|\bar{\boldsymbol{y}}\|_2 \leq y_0\} \tag{54}
$$

- the positive semi-definite cone:

$$\mathcal{K}_i = \{\boldsymbol{y} \text{ s.t. } \text{mat}(\boldsymbol{y}) \succeq 0\} \tag{55}$$

  where mat is the operator which transforms a vector of dimension $d(d+1)/2$ into a symmetric $d \times d$ matrix.

Depending whether $\mathcal{K}$ consists only of positive orthant, the resulting problem belongs to the class of *linear programming*, whereas if it contains also the second-order cones, it belongs to the class of *second-order cone programming*. In this work, 3D yield criteria of reinforced concrete naturally involve semi-definite constraints, as discussed before, so that the problem belongs to the broader class of *semi-definite programming*.

For such highly structured problems, efficient solvers based on primal-dual interior-point algorithms have been developed. We have implemented our own solver, following the implementation described in [Van10]. We refer the reader to the mentioned reference for more details on the algorithmic aspects.

Let us just mention that, in the course of the interior-point solver iterations, Newton systems involving both $\boldsymbol{x}, \boldsymbol{s}$ but also dual variables $\boldsymbol{y}$ and $\boldsymbol{z}$ respectively associated with the first two constraints in (51) must be solved. It is worth pointing out that primal $\boldsymbol{s}$ and dual $\boldsymbol{z}$ slack variables are involved in the definition of the yield condition in conic SDP form. As a result, such variables and the associated constraints are purely local to a given node. They can therefore be efficiently condensed when solving the Newton system. Similarly, the dual variable $\boldsymbol{y}$ essentially corresponds to the displacement unknowns $\boldsymbol{u}$ of the hybrid method. Static condensation of the stress variables present in $\mathbf{x}$ can also be performed when solving the Newton system, as discussed in the elastic case. As a result, solving the Newton system involves the resolution of a linear system of size approximately equal to the number of displacement unknowns. Accounting for the specific structure of the underlying optimization problem therefore enables to achieve a more efficient implementation, rather than using a black-box solver.

4 Numerical examples

In the following examples, the proposed formulation will be validated against other approaches including analytical solutions of simplified models (plates, truss analogies), experimental results, or other numerical solutions. Special attention will be paid to both cases of elastoplastic and limit analysis. For the latter, comparisons will be made against the kinematic upper-bound limit analysis approach of 3D reinforced concrete structure based on the work of [VABDB20] and which has been extended to account for 1D rebars instead of 3D smeared regions as considered in the original paper. In addition to providing an error estimation with respect to the proposed lower-bound static approach, kinematic results also offer an additional understanding of the underlying phenomena when inspecting the corresponding collapse mechanisms or plastic dissipation regions.

4.1 Rectangular concrete slab subjected to uniform load

In this section, we aim at validating our formulation in the context of concrete slabs under bending. The plastic theory of reinforced concrete has been widely studied using limit analysis approaches, the most notable being the yield line approach developed by Johansen [Joh62]. In [Mas67] analytical solutions for concrete slab subjected to uniform load have been derived.

Here, we compare our 3D equilibrium based approach with such analytical yield solutions based on a thin plate model. The example discussed is the square simply supported slab, uniformly loaded with $q = 1$ (fig.4). When considering a normal moment criterion (Johansen yield condition), the exact solution of such a square plate is given by $\alpha_{yieldLine} = 24m/a^2$, where m is the limit moment per meter and a the plate side length.

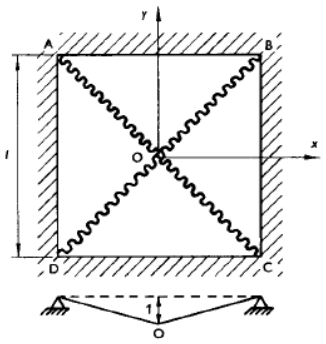

Figure 4: Simply supported square slab, uniformly loaded. Yield lines obtained in [Mas67].

With the proposed approach, a 3D model of a quarter of the plate is considered, taking into account symmetries. Vertical displacements are fixed for each point of the vertical faces and in-plane displacements are left free (fig.5).

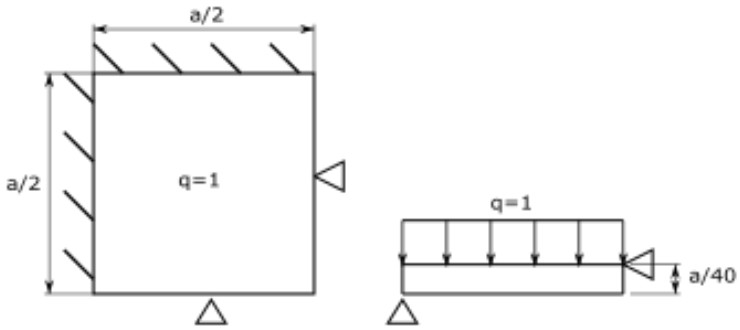

Figure 5: Slab model load an displacements conditions.

First of all, the case of a fully isotropic material is studied, in adequacy with the analytical solution. For this purpose, a Rankine criterion with $f_t = 20\,\text{MPa}$ and $f_c = 20\,\text{MPa}$ is considered. The geometry is a $2\,\text{m} \times 2\,\text{m}$ square slab of thickness 0.05 m. With such strength limitations the limit moment is $m = 12.5\,\text{kN/m}$, and therefore a theoretical scale factor $\alpha_{theo} = 0.075$ is expected for a uniform loading of $1\,\text{MN/m}^2$.

Five static lower-bound and kinematic upper-bound limit analysis (see 3.2) are computed from a very coarse mesh until a mesh consisting of 7911 tetrahedrons (see fig. 6).

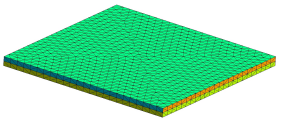

Figure 6: Fine mesh of the plate of 7911 tetrahedrons.

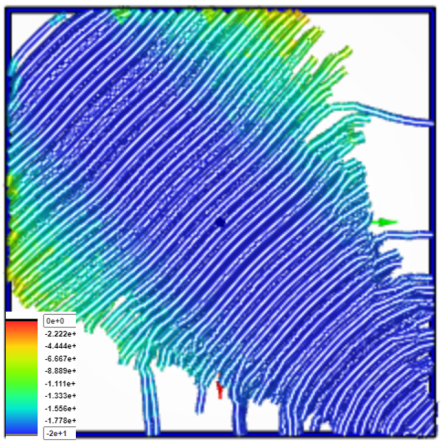

(a) Stress flow associated to the compressive limit strength (-20 MPa)

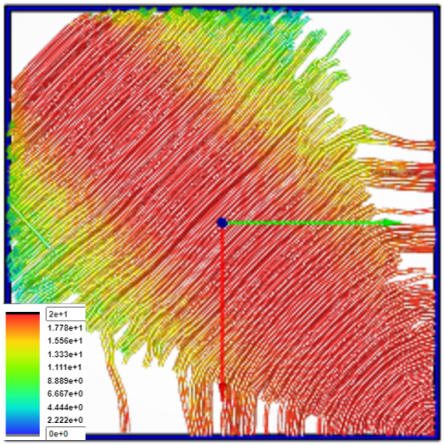

(b) Stress flow associated to the tensil limit strength (+20 MPa)

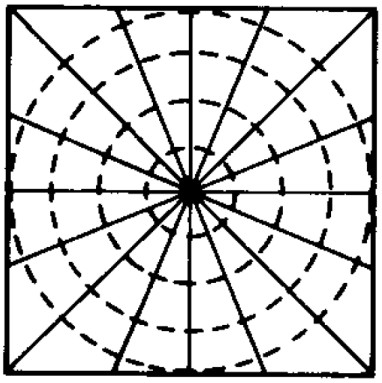

(c) First analytical distribution of moment equilibrating the failure loading according to [Mas67] (Prager radial field)

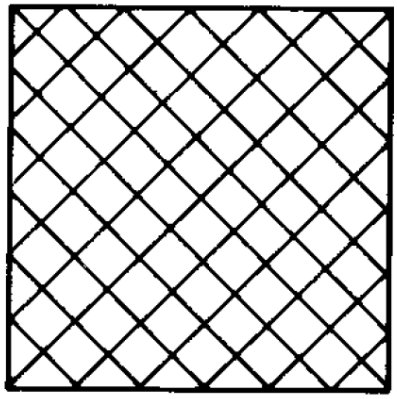

(d) Second analytical distribution of moment equilibrating the failure loading according to [Mas67] (Vallence's field)

Figure 7: Stress flows (a) and (b) compared to the analytical principal direction of moment (c) and (d).

Figures 7 (c) and 7 (d) are two static analytical solutions equilibrating the yield line factor prediction, thereby proving that the upper bound is the true failure loading. Those analytical fields stem from the work of Prager and Vallance, and, as explained in [Mas67], any linear combination of those two fields equilibrates the failure load.

On fig.9, we can see that the load factor bracketing of the two dual analysis converges towards a value close to the theoretical yield line solution. This good adequacy is confirmed by the compressive/tensile stress flow distribution which corresponds to a linear combination of the radial and diagonal analytical solutions (see fig. 7).

Finally, the generalised displacement obtained from the equilibrium computation are compared against those obtained from the kinematic upper bound approach (fig. 8). One can see that both 3D displacement fields are in good agreement and indeed correspond to the collapse mechanism expected from the theoretical yield line solution.

To illustrate the behavior of reinforcement, we then deal with the same example with $f_t = 2\,\text{MPa}$ and one layer of tensile reinforcements. The latter consist of 8 mm diameter bars with a spacing of 7 cm and concrete cover is 1 cm. Reinforcement are laid out parallel to the edges of the square slab in both directions. For such characteristics, the analytical limit moment becomes $m = 12.85\,\text{kN/m}$, and therefore a theoretical scale factor $\alpha_{theo} = 0.077$ is expected for a uniform loading of $1\,\text{MN/m}^2$. As for the homogeneous case, five computations are made from a very coarse mesh until a mesh composed of 7911 tetrahedrons. On fig.11, we can see that the load factor bracketing of the two dual analyses converges toward a value slightly superior than the analytical expectation but nevertheless very close (the gap between the kinematic upper bound and the theoretical value is less than 4

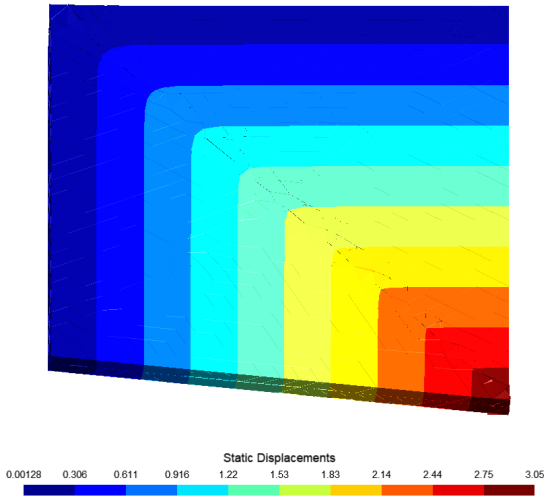

(a) Static generalized displacements

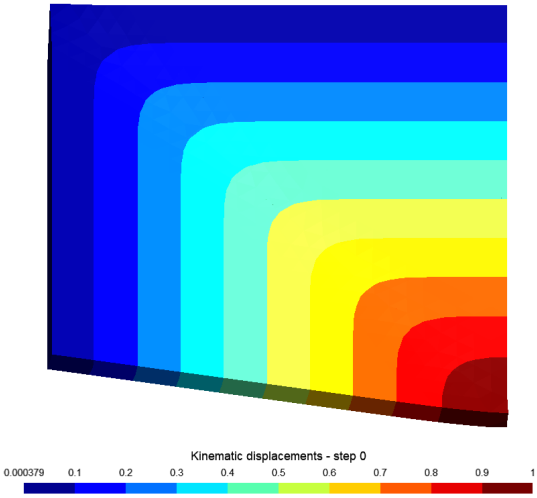

(b) Kinematic displacements

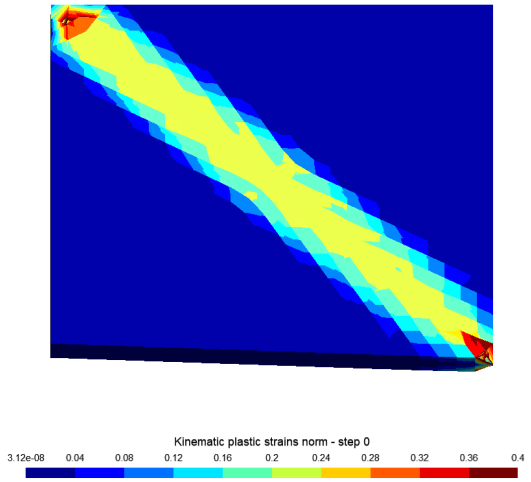

(c) Kinematic plastic strains

Figure 8: Displacements distribution obtained from the proposed static approach (a) compared to the kinematic solution (b). Kinematic strains (c) illustrate the same mechanism as the yield line solution.

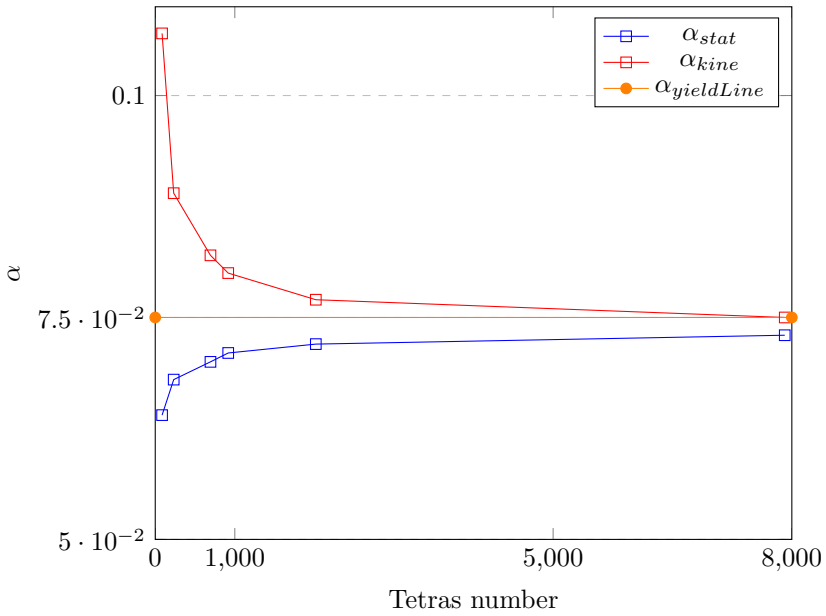

Figure 9: Amplification factor of the uniform loading to reach failure according to static analysis, kinematic analysis, yield line theory.

%). This difference can be explained by the anisotropy brought out by the reinforcements and the fact that the latter is model in a discrete manner rather than smeared over the whole region. The compression stress in concrete follows a slightly different pattern than the homogeneous case since it corresponds to the full radial analytical field. The tensile reinforcements are mobilized to equilibrate the tensile forces as expected (see fig. 10).

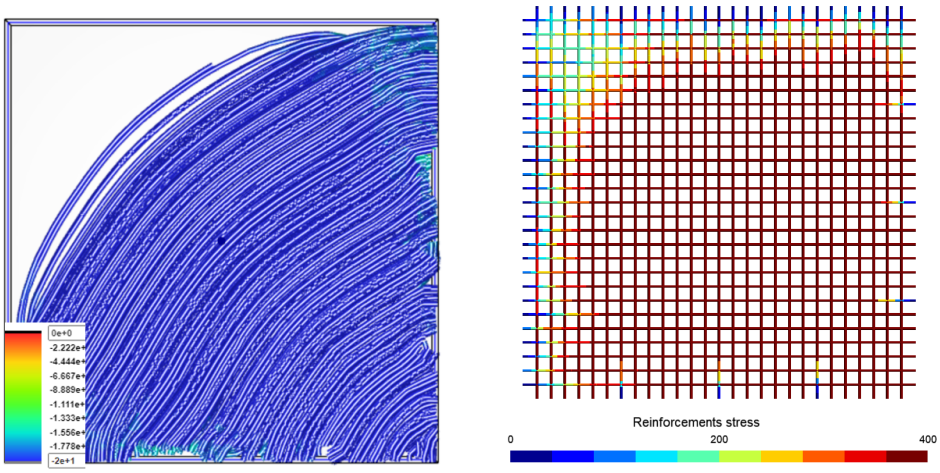

(a) Stress flow associated to the compressive limit strength (-20 MPa)

(b) Reinforcements stress

Figure 10: Stress compressive flow (a) and reinforcements stress (b).

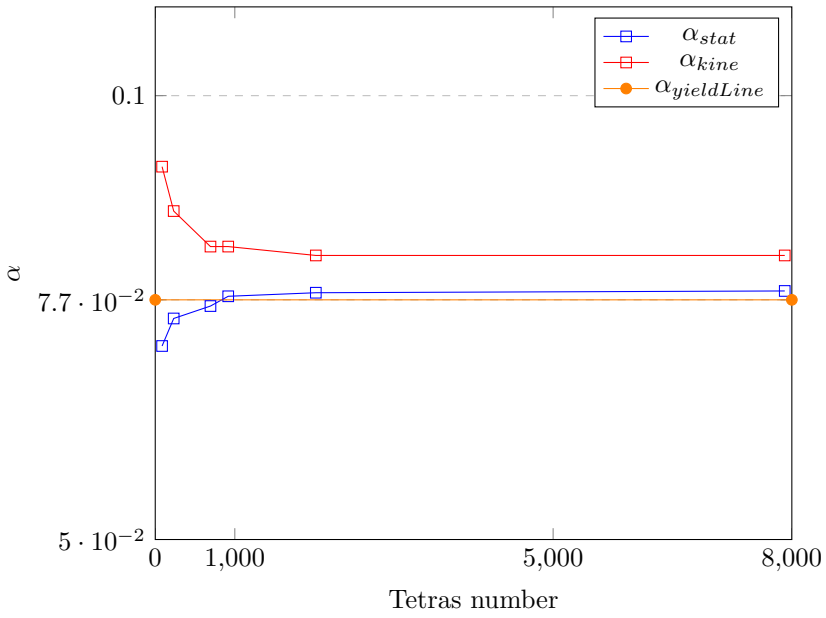

Figure 11: Amplification factor of the uniform loading to reach failure according to the static analyses, the kinematic analyses, and the yield line theory. Reinforcements are modeled thanks to embedded lines.

4.2 Lower bound of the collapse load of beams in bending

The article [TD02] aims to establish a curvature-moment law in adequacy with experimentation when RC beams are in the plastic range. Thus, 22 specimens of reinforced concrete beams are loaded experimentally until failure, all the specimens being one span simply supported RC beams. Two loading conditions (11 specimens each) were tested, although for our comparison we only focus on the case of a single concentrated loading at mid-span. Extensometers were placed in order to measure the strain in the vicinity of the maximal moment all along the loading process. The scale effect was investigated by testing three ranges of dimensions while slenderness and height to base ratio are kept constant. Longitudinal reinforcement ratio ranges between 0.28 to 1.70 and different stirrups spacing are tested.

Beam	B, mm	H, mm	L, mm	Tension reinforcement	Compression reinforcement	ρ, %	Stirrups diam/spacing mm/mm
T1A1	100	200	2000	1 ϕ 12	1 ϕ 8	0.56	1ϕ 6/150
T2A1	100	200	2000	2 ϕ 12	2 ϕ 8	1.13	1ϕ 6/150
T3A1	100	200	2000	3 ϕ12	2 ϕ8	1.70	1ϕ6/150
T4A1	200	400	4000	2 ϕ12	2 ϕ10	0.28	1ϕ6/200
T5A1	200	400	4000	4 ϕ12	2 ϕ10	0.56	1ϕ6/200
T6A1	200	400	4000	8 ϕ12	2 ϕ10	1.13	1ϕ6/200
T7A1	200	400	4000	12 ϕ12	2 ϕ10	1.70	1ϕ6/200
T8A1	300	600	6000	2 ϕ12	2 ϕ12	0.13	1ϕ6/150
T9A1	300	600	6000	4 ϕ12	2 ϕ12	0.25	1ϕ6/150
T10A1	300	600	6000	9 ϕ12	2 ϕ12	0.56	1ϕ6/150
T11A1	300	600	6000	18 ϕ12	2 ϕ12	1.13	1ϕ6/150

Table 1: Characteristics of specimens.

For the 11 mid-span loading specimens, we compute a lower bound collapse load thanks to our equilibrium finite-element limit analysis, taking into account the following assumptions:

- A Rankine yield criterion with $f_t = 0.1\,\text{MPa}$ and $f_c = 27\,\text{MPa}$ for the bulk concrete,
- A 1D perfectly plastic behaviour with $f_y = f_u = 672\,\text{MPa}$ for the reinforcements,
- The geometry complies with the description of table 1,
- A mesh of 3900 tetras (fig.12).

Concerning the boundaries conditions (see fig.13):

- All the mesh points of the extremity's faces have their generalized displacements linked to the 3 displacements and 3 rotation of the barycenter of the face. The imposed displacement are prescribed such that the three rotations are free and that each face vertical displacements are null. Transversal and longitudinal displacement are null at one of the two extremities to ensure stability.
- The vertical load is applied as a normal pressure at the middle of the beam, along a length $L_{load} = 0.1 \times L_{tot}$ and on the total width of the beam.

The first interesting set of values to observe consists of both the reinforcement stress and the stress compressive eigenvectors, as illustrated in figure 14. Compression struts at $f_c = 27\,\text{MPa}$ appear, as expected, while tensile reinforcements are mobilized to their limit strength of $f_y = f_u = 672\,\text{MPa}$. Stresses in stirrups do not reach their plastic limit since the experiment was designed in order to yield a flexural failure.

Integrating the stress state resulting from the limit analysis computation, we can evaluate the difference between our numerical predictions and the experimental moment measured at collapse thanks to sensors. The comparison is shown on Fig. 15, 16, 17 for each type of dimension as a

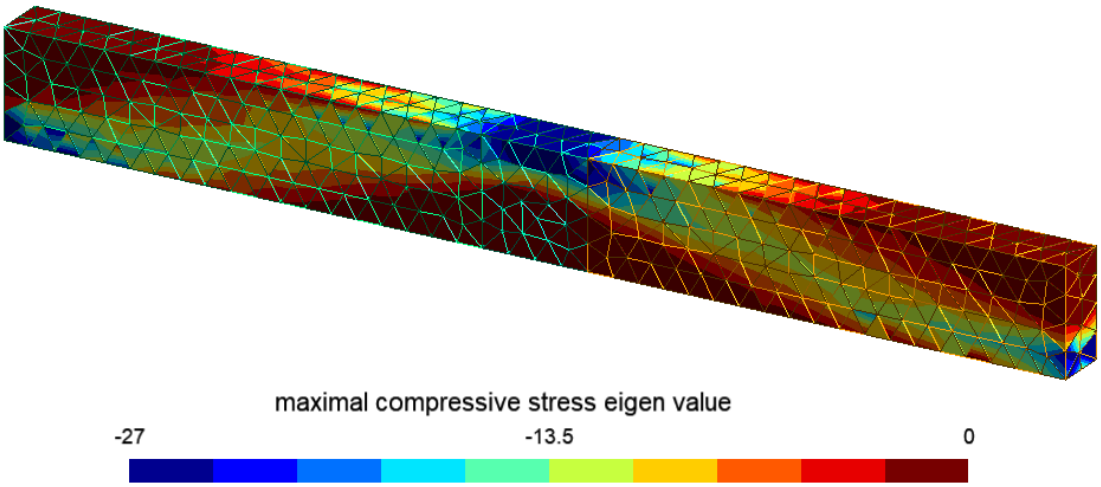

Figure 12: Mesh composed of 3900 tetrahedrons, specimen T_6.

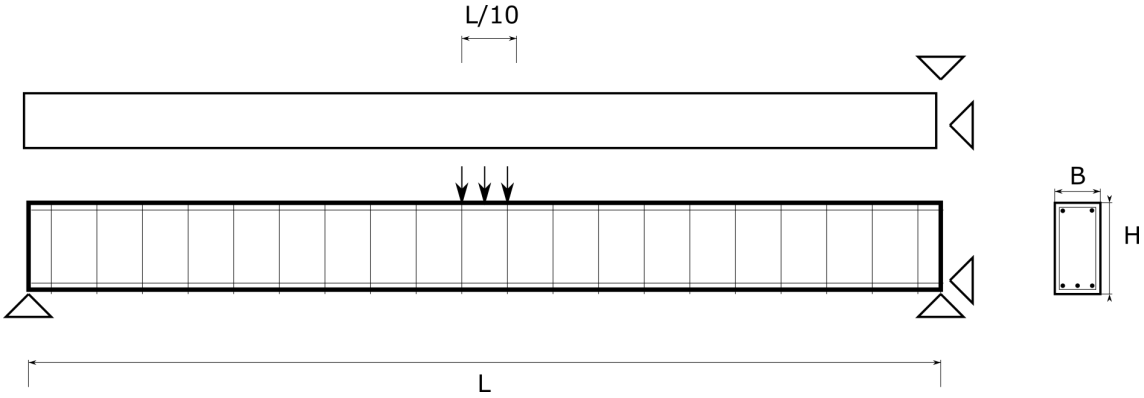

Figure 13: General geometry and loading of test cases.

function of the longitudinal reinforcement ratio. We see that numerical and experimental values are in broad agreement for all the specimens except for T_7 and T_{11}, for which the collapse load is overestimated by respectively 5% and 10%.

It turns out that this overestimation is a consequence of the assumption made regarding the concrete constitutive law. Indeed, by assuming a rigid plastic behaviour, we disregard the possibility of any failure resulting from a limitation of the concrete strains in compression. However, it appears that the two specimens with a particularly high tensile reinforcement ratio, precisely T_7 and T_{11}, failed because of the concrete crushing limitation. A safeguard regarding this crushing limitation would be to analyse the compressive strains resulting from the kinematic elastoplastic analysis (whom theory is not described in this article but can partly be found in [VABDB20]).

The premature failure observed for a high ratio of reinforcement is actually a direct consequence of the physical framework we assumed in this paper. In [MS72], a very general reflection is made on the use of associated perfect plasticity to model reinforced concrete. As it is pointed out by Save and Massonet (chap. 3.2.3), for a high ratio of reinforcement, plastic rotation capacity decreases and can even disappear if the concrete fails by crushing before the plastic behavior in reinforcement is reached. In this case, the plastic redistribution needed to reach the failure mechanism predicted by limit analysis is not possible and our numerical prediction overestimates the failure loading.

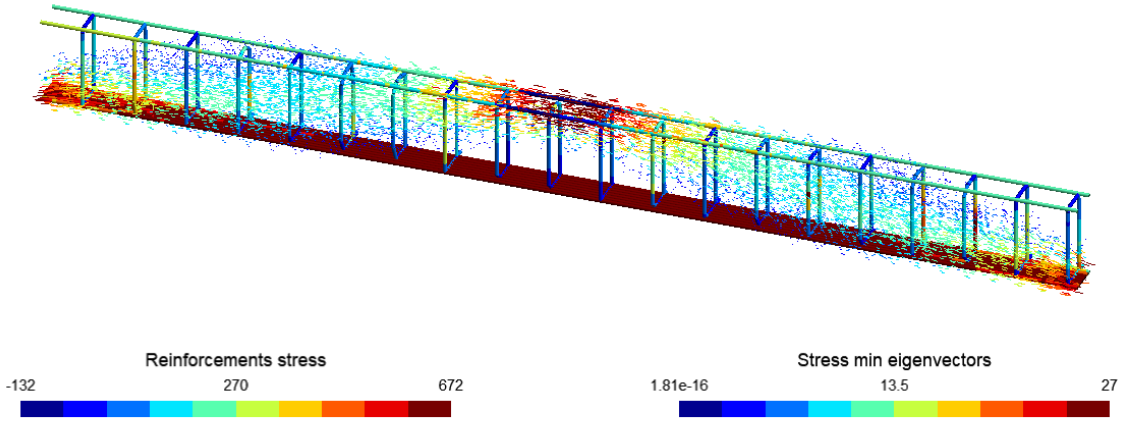

Figure 14: Lower bound limit analysis results: stress in reinforcements and compressive eigenvectors in concrete, specimen T_6.

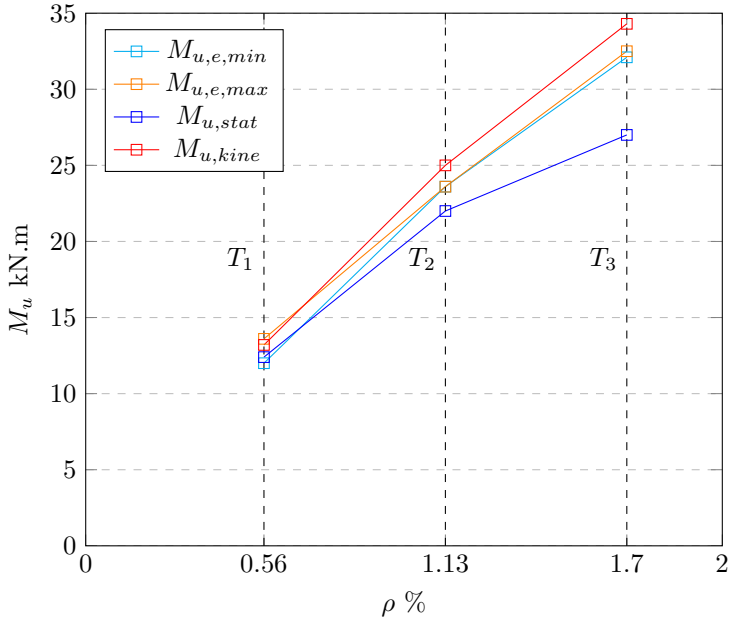

Figure 15: Collapse moment at mid-span for half-size specimen T_1, T_2, T_3

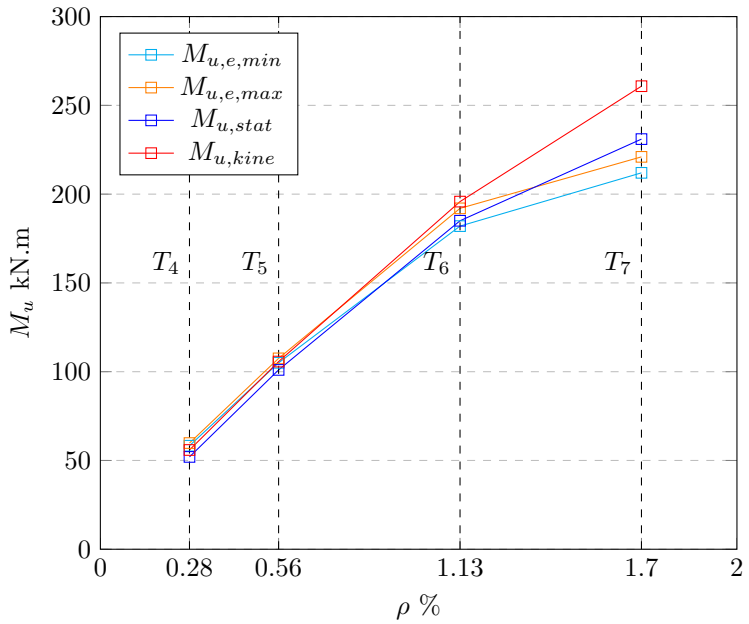

Figure 16: Collapse moment at mid-span for full-size specimen T_4, T_5, T_6, T_7

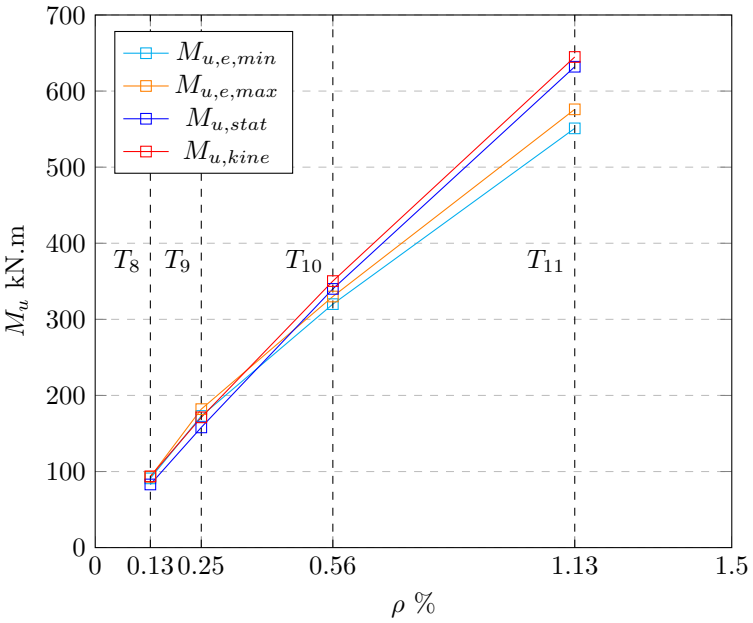

Figure 17: Collapse moment at mid-span for double-size specimen T_8, T_9, T_{10}, T_{11}

4.3 Torsional behavior of a rectangular cross section

In this section the torsional behavior of a RC beam is discussed. In [LT72], a failure model using a space truss analogy is presented and applied to the case of combined torsion and bending of RC beam. In this example, we will only deal with the case of pure torsion for simplicity.

On Figure 18, the failure model for reinforced concrete beams subjected to torsion and applicable to general cross sectional shapes established in [LT72] is presented.

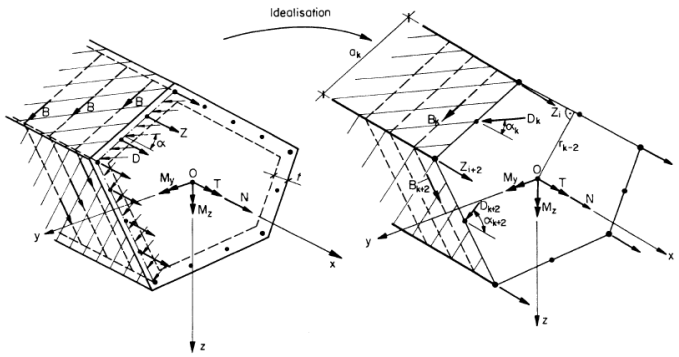

Figure 18: Failure Model - Space Truss with Variable inclinations of the Diagonals (ref [LT72]).

This failure model consists of longitudinal reinforcement considered to be concentrated into stringers at the corner and intermediate shear walls. Stirrups act as posts and the concrete between the inclined cracks provides the compression diagonals. The angle of the diagonal α is taken to be constant for each side. The assumption of an under-reinforced section is made so that the failure is determined by the yield force of the longitudinal stringers or the stirrups. This assumption is needed to comply with the ductility requirement of the theory of plasticity. Indeed, as it has already been discussed, the case of a concrete failure by crushing is beyond the scope of a perfectly plastic material.

For a rectangular cross section in pure torsion, when the failure is due to the yielding of both stringers and stirrups, the followings results hold:

- The inclination of the compression diagonal α is determined by the proportion of transverse reinforcement yield force compared to the longitudinal one. The following equality holds:

$$\tan^2(\alpha) = \frac{F_{st}}{s}\frac{u}{F_l} \tag{56}$$

  where F_{st} and F_l are respectively the force supported by one stirrup and all the longitudinal reinforcement at yielding, s the stirrups spacing, and u the cross section perimeter.

- The ultimate torque responsible for the yielding of the total amount of reinforcements is:

$$T_{u0} = 2A_0\sqrt{\frac{F_{st}}{s}\frac{u}{F_l}} \tag{57}$$

For this failure mechanism, it is possible to evaluate the compression stress in the strut. Indeed, the concrete compression diagonals carry the force determined by the truss equilibrium. Moreover, as explained in [LT72], a beam with a solid cross section has the same failure mode as a corresponding hollow section with thickness given by $t = min(b/6, (b-2c)/5)$ with b the width of the section and c the concrete cover of the stirrups. Knowing this effective thickness, it becomes possible to evaluate the compressive stress thanks to the equilibrium equation:

$$\sigma_c = -\frac{T_{u0}}{2At}\frac{1}{\sin(\alpha)\cos(\alpha)} \tag{58}$$

To check the ability of our variational formulation and numerical implementation to tackle this problem, we compare our numerical predictions to this analytical model for 3 particular RC beams with a square cross section. The assumptions common to the three models are:

- $f_t = 0.1\,\text{MPa}$ and $f_c = 50\,\text{MPa}$. A large value of compressive strength is chosen so that the failure mechanism does not imply concrete crushing.

- The cross section dimensions : $b = 36\,\text{cm}$, $h = 72\,\text{cm}$ and $c = 4.5\,\text{cm}$.

- Longitudinal reinforcements are placed at corner and intermediate shear walls.

- Stirrups of different diameters and spacing are laid out all along the beam.

Computations are made for 3 different reinforcement ratio (stirrups density/longitudinal density):

Model	Longitudinal reinforcements	Stirrups diam/spacing mm/mm	T_{u0} (MN.m)	α (deg.)	σ_c (MPa)
A	8 ϕ25	1 ϕ8 / 2.7 cm	0.27	45	30
B	8 ϕ25	1 ϕ8 / 6 cm	0.18	34	21
C	8 ϕ25	1 ϕ12 / 3.1 cm	0.38	55	44

Table 2: Reinforcements characteristics and expected values of the 3 numerical models

We first analyze the three models mesh convergence with respect to the corresponding analytical prediction in Fig. 19. Clearly, the limit load prediction seems to converge to a value close to the analytical prediction for all three models.

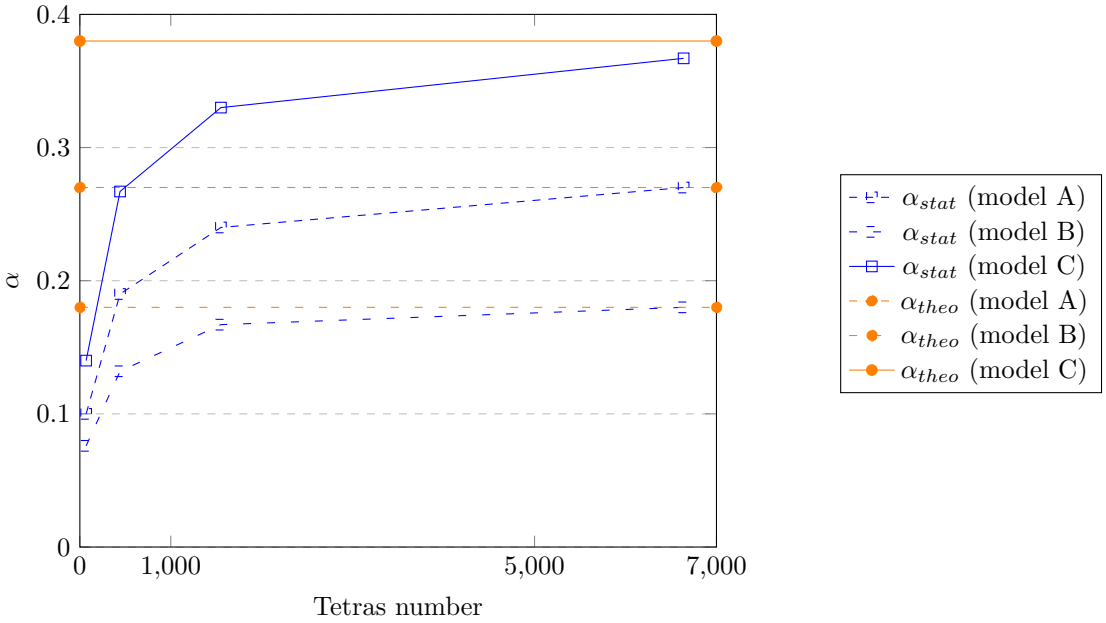

Figure 19: Limit torque for each model.

The generalized displacements correspond to the expected mechanism in pure torsion (fig. 20), and the static stresses in reinforcements confirm the overall yielding of the reinforcement (fig. 21). For the model A, the direction of struts concentrated in shear wall are in broad agreement with the 45° analytical prediction for each panel, and the predicted value of 30 MPa is observed (fig 22).

The evolution of the struts inclination according to the reinforcements ratio, is shown on fig.23. On those pictures, the predicted values for models A, B and C are retrieved.

Dealing for instance with the model A, it is possible to assess the evolution of the tangent stiffness all along the loading path from 0 to the limit torque value of 0.27 MN.m using the elastoplastic formulation (the Young's modulus is 22 GPa and the Poisson's ratio is 0.3). For this purpose, we draw a load-displacement curve (ref. fig. 24), where the "displacement" is actually the beam axial rotation obtained at the loading step. It turns out that the reinforcements yielding begins for a loading torque comprised between 0.2 MN.m and 0.25 MN.m. The plastic flaw appears clearly for the last increment of 0.01 MN.m until the ultimate value given by limit analysis.

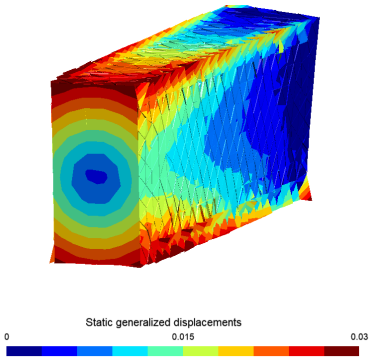

Figure 20: Generalized displacements in pure torsion given by the static yield analysis. Model A (6639 Tetras).

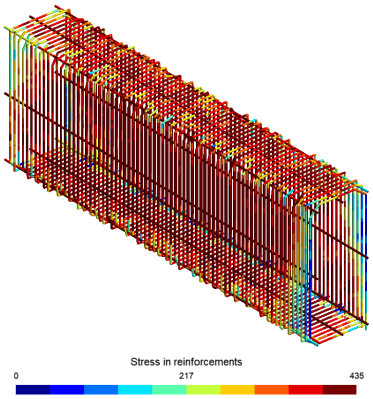

Figure 21: Stress in reinforcement. Model A (6639 Tetras).

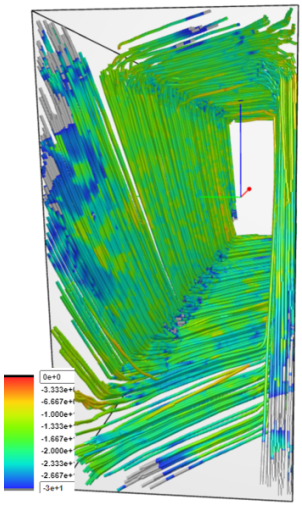

Figure 22: Stress compression flow corresponds to the analytical prediction: the different subpanels share the same angle of inclination (45°) and the struts are concentrated in shear walls. Model A (6639 Tetras).

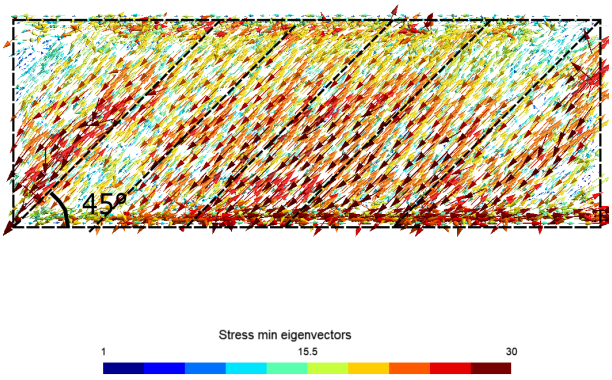

(a) Model A : $\alpha = 45$ and $\sigma_c = 30MPa$

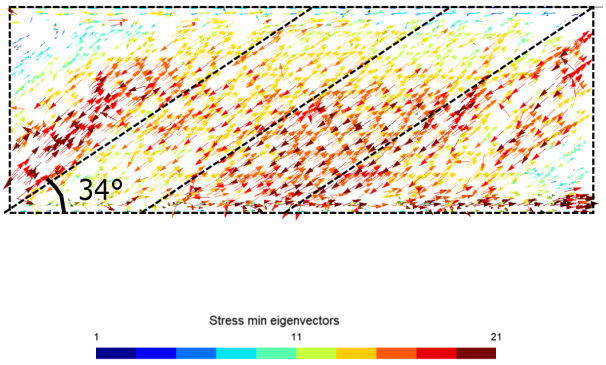

(b) Model B : $\alpha = 34$ and $\sigma_c = 21MPa$

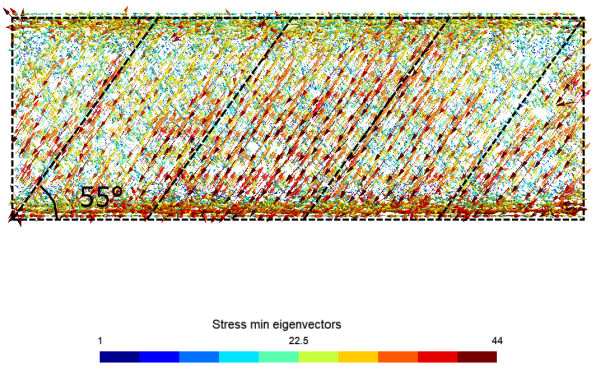

(c) Model C : $\alpha = 55$ and $\sigma_c = 44MPa$

Figure 23: Evolution of the compression diagonal inclination and concrete maximal compression stress value for the 3 models. Analytical predictions are retrieved.

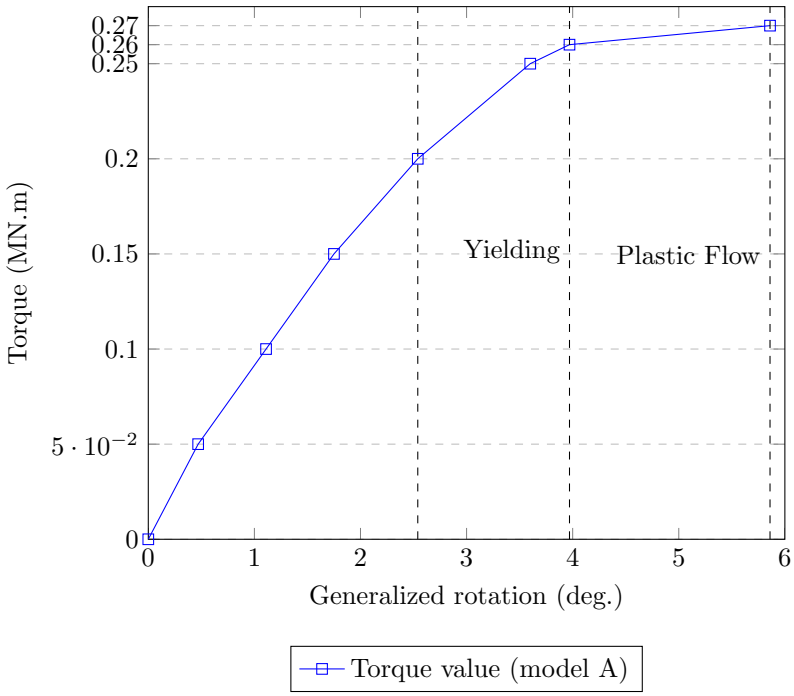

Figure 24: Limit torque for each model

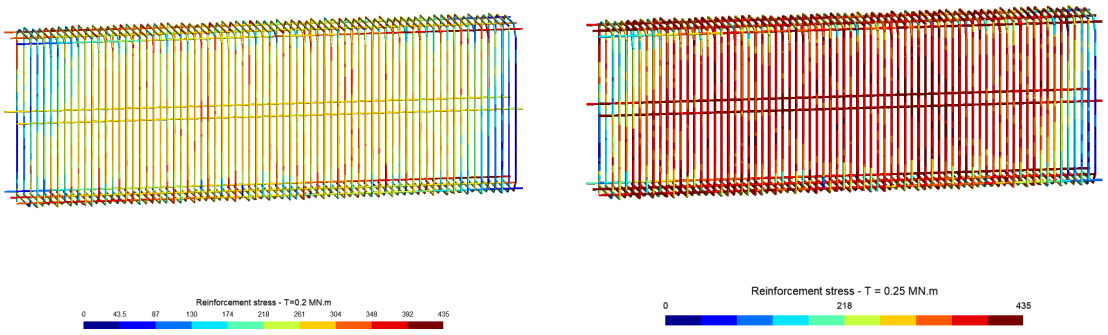

(a) Model A : Stress in reinforcement load step T = 0.2 MN.m. Neither bar is yielding.

(b) Model A : Stress in reinforcement load step T = 0.25 MN.m. Stirrups and longitudinal bars begin to yield.

Figure 25: Stress evolution in reinforcements at the two loading steps bracketing the beginning of plastic behaviour.

5 Conclusion

We have presented in this work a new 3D equilibrium-based finite element formulation for reinforced concrete, dual to the more classical displacement-based formulation. The rebars are considered as 1D elements embedded into the 3D concrete volume. The exact geometrical definition of the rebars is thus needed, and not only the reinforcement ratio for each direction, as needed in homogenization-based methods.

The main novelty is, firstly, the proposed method to connect the axial rebar stress with the 3D concrete stresses, in the framework of an equilibrium-based formulation, strongly ensuring the equilibrium in the solids' volume. Secondly, it is the use of the SDP optimization framework to solve the elastoplastic and limit analysis problems of a reinforced concrete material. For a mesh with linear tetrahedra, the rebars are attached to the concrete by linking their axial displacement to the one of the triangular faces of the mesh. Hence, the statical equilibrium at each face will be assured, considering both the rebar and the concrete stresses.

For the elastic case, the equilibrium-based formulation was proven to be equivalent to an optimization problem, extended to the elastoplastic case by simply adding SDP constraints for the concrete stress (Rankine or truncated Mohr-Coulomb), and linear constraints for the rebar stress. The non-linear SDP optimization problem is then solved using an interior point algorithm.

As it can be seen from the numerical examples presented in the second part of this work, the proposed approach has proven to be very efficient in solving various reinforced concrete elastoplastic problems, and successfully providing a limit load, even for large dimension problems. Thus, this approach represents a reliable alternative to the more rudimentary strut and tie method, and that can be used in the conception and validation phases of a reinforced concrete structure.

Giving access to a dual approach, this equilibrium formulation opens the door to constitutive law error estimation. Using this error assessment, a remeshing scheme could be established in order to reduce the problem size and therefore enhance the efficiency of the resolution.

References

[2219] Limitstate, limitstate:slab manual, 2nd edition. 2019.

[AA38] Gvozdev AA. The determination of the value of the collapse load for statically indeterminate systems undergoing plastic deformation. *Proceedings of the Conference on Plastic Deformations, Akademiia Nauk SSSR, Moscow*, pages 19–33, 1938.

[APO21] Mads Emil Møller Andersen, Peter Noe Poulsen, and John Forbes Olesen. Finite-element limit analysis for solid modeling of reinforced concrete. *Journal of Structural Engineering*, 147(5), 2021.

[APO22] Mads Emil Møller Andersen, Peter Noe Poulsen, and John Forbes Olesen. Partially mixed lower bound constant stress tetrahedral element for finite element limit analysis. *Computers & Structures*, 258:106672, 2022.

[BP07] Christos D Bisbos and Panos M Pardalos. Second-order cone and semidefinite representations of material failure criteria. *Journal of Optimization Theory and Applications*, 134(2):275–301, 2007.

[CCJS14] Vladimir Cervenka, Jan Cervenka, Libor Jendele, and Vit Smilauer. Atena simulation of crack propagation in concrack benchmark. *European journal of environmental and civil engineering*, 18(7):828–844, 2014.

[D20] Ferreira D. Diana user manual, release 10.4. 2020.

[dAM17] JP Moitinho de Almeida and Edward A Maunder. *Equilibrium finite element formulations*. John Wiley & Sons, 2017.

[DPG52] DC Drucker, W Prager, and HJ Greenberg. Extended limit design theorems for continuous media. *Quarterly of applied mathematics*, 9(4):381–389, 1952.

[EBBA+20a] Chadi El Boustani, Jérémy Bleyer, Mathieu Arquier, Mohammed-Khalil Ferradi, and Karam Sab. Dual finite-element analysis using second-order cone programming for structures including contact. *Engineering Structures*, 208:109892, 2020.

[EBBA+20b] Chadi El Boustani, Jeremy Bleyer, Mathieu Arquier, Mohammed-Khalil Ferradi, and Karam Sab. Elastoplastic and limit analysis of 3d steel assemblies using second-order cone programming and dual finite-elements. *Engineering Structures*, 221:111041, 2020.

[En92] BS En. En 1992-1-1: 2004 eurocode 2: Design of concrete structures. *General rules and rules for buildings*, 3, 1992.

[FdV65] Baudouin Fraeijs de Veubeke. Displacement and equilibrium models in the finite element method. *Stress analysis*, pages chapter–9, 1965.

[GRM88] TB Griffin, Bathmanathan Dayanand Reddy, and John Brand Martin. A numerical study of holonomic approximations to problems in plasticity. *International Journal for Numerical Methods in Engineering*, 26(6):1449–1466, 1988.

[Hc54] H Hai-chang. On some variational principles in the theory of elasticity and the theory of plasticity. *Acta Physica Sinica*, 10(3):259, 1954.

[Joh62] Knud Winstrup Johansen. *Yield-line theory*. Cement and Concrete Association, 1962.

[Joh72] Knud Winstrup Johansen. *Yield-line formulae for slabs*. CRC Press, 1972.

[KDB10] Martin Kempeneers, Jean-François Debongnie, and Pierre Beckers. Pure equilibrium tetrahedral finite elements for global error estimation by dual analysis. *International Journal for Numerical Methods in Engineering*, 81(4):513–536, 2010.

[Kem06] Martin Kempeneers. Eléments finis statiquement admissibles et estimation d'erreur par analyse duale. *Mémoire de thèse doctorat Université de Liège Faculté des Sciences Appliquées*, 31, 2006.

[KLS07] K Krabbenhøft, AV Lyamin, and SW Sloan. Formulation and solution of some plasticity problems as conic programs. *International Journal of Solids and Structures*, 44(5):1533–1549, 2007.

[KLSW07] K Krabbenhoft, AV Lyamin, SW Sloan, and P Wriggers. An interior-point algorithm for elastoplasticity. *International Journal for Numerical Methods in Engineering*, 69(3):592–626, 2007.

[LPN12] Kasper P Larsen, Peter N Poulsen, and Leif O Nielsen. Limit analysis of 3d reinforced concrete beam elements. *Journal of engineering mechanics*, 138(3):286–296, 2012.

[LT72] Paul Lampert and Bruno Thürlimann. Ultimate strength and design of reinforced concrete beams in torsion and bending. In *Ultimate Strength and Design of Reinforced Concrete Beams in Torsion and Bending/Résistance et dimensionnement des poutres en béton armé soumises à la torsion et à la flexion/Bruchwiderstand und Bemessung von Stahlbetonbalken unter Torsion und Biegung*, pages 107–131. Springer, 1972.

[Mak10] Athanasios Makrodimopoulos. Remarks on some properties of conic yield restrictions in limit analysis. *International Journal for Numerical Methods in Biomedical Engineering*, 26(11):1449–1461, 2010.

[Mas67] Ch. Massonnet. Complete solutions describing the limit state of reinforced concrete slabs. *Magazine of Concrete Research*, 19(58):13–32, 1967.

[MdAR96] EAW Maunder, JP Moitinho de Almeida, and ACA Ramsay. A general formulation of equilibrium macro-elements with control of spurious kinematic modes: the exorcism of an old curse. *International Journal for Numerical Methods in Engineering*, 39(18):3175–3194, 1996.

[MM06] A Makrodimopoulos and CM Martin. Lower bound limit analysis of cohesive-frictional materials using second-order cone programming. *International Journal for Numerical Methods in Engineering*, 66(4):604–634, 2006.

[MM08] Christopher M Martin and Athanasios Makrodimopoulos. Finite-element limit analysis of mohr–coulomb materials in 3d using semidefinite programming. *Journal of engineering mechanics*, 134(4):339–347, 2008.

[MS72] C. Massonet M. Save. Plasticity and viscosity. *IABSE Congress Report*, 1972.

[Mö08] E Mörsch. Reinforced concrete construction, theory and application (der eisenbetonbau, seine theorie und andwendung). *Verlag von Konrad Wittwer*, 1908.

[NH16] Mogens Peter Nielsen and Linh C Hoang. *Limit analysis and concrete plasticity*. CRC press, 2016.

[PT72] Theodore HH Pian and Pin Tong. Finite element methods in continuum mechanics. *Advances in applied mechanics*, 12:1–58, 1972.

[Rit99] W Ritter. The hennebique construction method. *Schweizerische Bauzeitung*, V. XXXIII(7):41–61, 1899.

[RM07] Miguel Fernández Ruiz and Aurelio Muttoni. On development of suitable stress fields for structural concrete. *ACI Structural Journal*, 104(4):495, 2007.

[SSJ87] Jorg Schlaich, Kurt Schäfer, and Mattias Jennewein. Toward a consistent design of structural concrete. *PCI journal*, 32(3):74–150, 1987.

[TD02] M. Taliano and Piergiorgio Debernardi. On evaluation of rotation capacity of reinforced concrete beams. *Aci Materials Journal*, 99:360–368., 05 2002.

[TT02] Kuchma DA Tjhin TN. Computer-based tools for design by strut-and-tie method: Advances and challenges. *ACI Structural Journal*, 99(5):586–94, 2002.

[VABdB18] Hugues Vincent, Mathieu Arquier, Jeremy Bleyer, and Patrick de Buhan. Yield design-based numerical analysis of three-dimensional reinforced concrete structures. *International Journal for Numerical and Analytical Methods in Geomechanics*, 42(18):2177–2192, 2018.

[VABDB20] Hugues Vincent, Mathieu Arquier, Jeremy Bleyer, and Patrick De Buhan. Numerical upper bounds to the ultimate load bearing capacity of three-dimensional reinforced concrete structures. *International Journal for Numerical and Analytical Methods in Geomechanics*, 44(16):2216–2240, November 2020.

[Van10] Lieven Vandenberghe. The cvxopt linear and quadratic cone program solvers. *Online: http://cvxopt. org/documentation/coneprog. pdf*, 2010.

[Was68] K. Washizu. Variational methods in elasticity and plasticity. *The Aeronautical Journal*, 72(694):889–889, 1968.

[Zha09] Shangyou Zhang. A family of 3d continuously differentiable finite elements on tetrahedral grids. *Applied Numerical Mathematics*, 59(1):219–233, 2009.